



ASME Accepted Manuscript Repository

Institutional Repository Cover Sheet

*First*

*Last*

ASME Paper Title: Large Eddy Simulations for Film Cooling Assessment of Cylindrical and Laidback Fan-Sholes with Reverse Injection

Authors: Ashutosh Kumar Singh, Kuldeep Singh, Dushyant Singh, Niranjan Sahoo

ASME Journal Title: Journal of Thermal Science and Engineering Applications

Volume/Issue \_13/3\_ Date of Publication (VOR\* Online) Nov 11 2020

ASME Digital Collection URL: <https://asmedigitalcollection.asme.org/thermalscienceapplication/article/13/3/03102>:  
-Eddy-Simulations-for-Film-Cooling-Assessment

DOI: [10.1115/1.4048679](https://doi.org/10.1115/1.4048679)

\*VOR (version of record)



**LARGE EDDY SIMULATIONS FOR FILM COOLING ASSESSMENT OF  
CYLINDRICAL AND LAIDBACK FAN-SHAPED HOLES WITH REVERSE  
INJECTION**

**Mr. Ashutosh Kumar Singh**

Trainee Teacher

Department of Mechanical Engineering

National Institute of Technology Manipur

Imphal, Manipur – **795 004 (India)**.

**Dr. Kuldeep Singh**

Senior CFD Research Fellow

Gas Turbine and Transmissions Research Centre

Nottingham University- NG7 2TU (**United Kingdom**).

**Dr. Dushyant Singh\***

\*Corresponding author,

Assistant Professor,

Department of Mechanical Engineering,

National Institute of Technology, Manipur

Imphal, Manipur – **795 004 (India)**

Email ID: [dushyant7raghu@gmail.com](mailto:dushyant7raghu@gmail.com) & [dushyant@nitmanipur.ac.in](mailto:dushyant@nitmanipur.ac.in)

**Dr. Niranjan Sahoo**

Professor

Department of Mechanical Engineering,

Indian Institute of Technology, Guwahati

Assam – **781 039 (India)**

## Abstract

The large eddy simulations (LES) are performed to access the film cooling performance of cylindrical and shaped hole for forward and reverse injection configurations. In the case of reverse/backward injection, the secondary flow is injected in such a way that its axial velocity component is in the direction opposite to mainstream flow. The study is carried out for a blowing ratio;  $M = 1$ , Density ratio;  $DR = 2.46$ , and injection angle;  $\alpha = 35^\circ$ . Formation of counter-rotating vortex pair (CRVP) is one of the major issues in the film cooling. This study revealed that the CRVP found in the case of forward cylindrical hole which promotes coolant jet “lift-off” is completely mitigated in the case of the reverse shaped hole. The coolant coverage for reverse cylindrical and reverse shaped holes are uniform and higher. The reverse shaped hole shows promising results among investigated configurations. The lateral averaged film cooling effectiveness of reverse shaped hole is 1.16 to 1.42 times higher as compared to the forward shaped holes. The improvement in the lateral averaged film cooling effectiveness of reverse cylindrical (RC) injection over forward cylindrical (FC) injection is 1.33 times to 2 times.

**Keywords:** Film cooling; large eddy simulations; cylindrical hole; shaped hole; afterburner of aero engine.

## 1. Introduction

The turbine entry temperature of modern gas turbine engines used for aviation has increased significantly over the years in order to improve the thermal efficiency and power output. Moreover, the demand for thrust in the case of fighter planes for some specific situations (like combat or take-off from small run-ways) is very high. This demand is fulfilled by burning of

additional fuel in the after-burner section. Because of the burning of the additional fuel inside the afterburner chamber, the temperature of this section increases further to 2200 K. *The* components in the pathway of hot flue gases exposed to very high temperature. The component under such high thermal loads and stress, needs a sophisticated cooling technique to ensure the allowable metal temperature for the safe operation.

Film cooling is an extensively effective technique in which a coolant or secondary fluid is injected through the row of holes over the surface[1]. The coolant stream forms a thin protective layer in-between hot flue gases and the surface to be protected. As the coolant jet enters the cross flow region due to the combined effect of pressure and shear forces, it splits into two counter-rotating vortex pair which is often referred to as “kidney vortices” [2]. Many researchers have studied the formation of vortices for the cross-flow jet [3,4]. The physical phenomenon of film cooling (Fig. 1) can be well understood from reference [5] . Mainly four types of vortices are identified in the film cooling viz. jet shear vortices, wake vortices, horseshoe vortices and kidney vortices [6,7]. It is visualised that the formation of “kidney vortices” promotes the coolant separation from the surface and improved mixing with hot mainstream [8–10]. In order to improve the coolant coverage and film cooling effectiveness, kidney vortices must be minimised or suppressed. Among all the known parameters that influence the formation of kidney vortices, the coolant-hole geometry is most important.

Last few decades research has been focused on different hole configuration to minimise the formation of kidney vortex in the flow field [11]. Goldstein et al. [5] was the pioneer to suggest the shaped hole of cylindrical nature at initial length and  $10^\circ$  expended angle at the exit. They found a remarkable increase in the film cooling effectiveness downstream of the hole. Haven et al. [9] experimentally studied three different holes viz. diffusion hole, conical diffuser and lateral diffusion configuration for fixed density ratio ( $DR = 1$ ). They reported that

the shaped hole generates another pair of vortex having the opposite sense of rotation. These vortices counter the jet-lift off the effect of “kidney vortices” and hence named as an “anti-kidney vortex”. Sauwamber et al. [12] have conducted a comprehensive experimental study over the three different hole configuration viz. cylindrical, fan-shaped (expanded in span-wise) and laidback fan-shaped (expanded in both stream-wise and span-wise). This study was conducted for density ratio (0.59), blowing ratio (0.5-2.5) and turbulence intensity (3.6-11%). This study revealed that the film cooling performance of shaped holes was better as compared to cylindrical holes. Because of the extended area at hole-exit, the momentum of the secondary fluid leaving the hole was lower; it reduced the secondary jet penetration into the mainstream and the flow lift off even at higher blowing ratio.

The film cooling over the flat surface with three different holes (cylindrical, laterally expanded, laterally-forward expanded) was studied with  $DR = 1$ ,  $M = 1$  and Reynolds number ( $Re = 5.2 \times 10^4$ ) based on the mainstream inlet geometry [13]. It was found that the film cooling effectiveness of laterally-forward expanded hole was the best among the investigated cooling hole configurations. The performance of laterally expanded cooling holes lies in between the cylindrical and laterally forward diffused holes. Bell et al. [14] experimentally investigated the film cooling with various hole configurations viz: cylindrical round simple angle, laterally diffuse simple angle, laterally diffuse compound angle, forward diffuse simple angle, forward diffuse compound angle. They noticed that all the simple holes showed better span-wise film cooling effectiveness as compared to compound angle holes. Dungal et al. [15] introduced a more simplified geometry commonly known as “branch hole configuration”. They observed that branching of hole minimises the detrimental effect of kidney vortex pair that further improves coolant coverage in the lateral direction. Ely et al. [16] numerically studied the film cooling over the flat plate with the noble sister hole configuration. They found that the vortices generated from the branches try to diminish the impact of the vortex generated by the hole.

One of the recent enhancement in film cooling area is the use of backward injection that allows improving the film cooling significantly by using simple hole configuration. Wu et al. [17] have carried out an experimental investigation in order to study the effect of blowing ratio over the performance of sister hole configuration. The results suggested that both at low blowing ratio ( $M = 0.5$ ) and high blowing ratio ( $M = 2$ ), the film cooling performance was improved.

Shetty et al. [18] carried out a numerical study of film cooling with backward injection over the aerofoil surface. They concluded that film cooling lateral effectiveness for backward injection was significantly higher than forward injection. Chen et al. [19] numerically studied the backward injection for three-hole configuration viz. simple cylindrical, fan-shaped and compound hole for the flat surface. The study was conducted for the blowing ratio (0.3 to 3), turbulence intensity (0.5 to 6%) and density ratio (1 to 2). They reported improved laterally averaged effectiveness for the backward injection simple cylindrical and compound hole, however reverse fan-shaped hole gave lower film cooling effectiveness. Singh et al. [20] experimentally and numerically investigated forward and reverse hole film cooling over the flat plate. The blowing ratio was varied from 0.25 to 5 and the density ratio was kept fixed at 0.91 for all angle of injection ( $30^\circ$  to  $60^\circ$ ). They found a remarkable increase in film cooling effectiveness at all the blowing ratios. The kidney vortices observed in the case of the forward cooling hole were totally eliminated with the use of the reverse hole and eventually significant gain in film cooling effectiveness is observed.

Tyagi et al. [21] and Acharya et al. [22] found that turbulence modelling using RANS is inefficient, especially in the wake region where RANS model under predicts quantities such as turbulent stress tensor and flow spreading in lateral direction and over predict the flow penetration in the vertical direction. As a consequence, RANS modelling over-predicts the centreline film-cooling and under-predicts the lateral spread of secondary fluid. The size of

kidney vortices is also not predicted accurately using RANS modelling. Moreover, direct numerical simulations are numerically accurate but computationally expensive for the range of Reynolds number typically found in aero-engines [23]. Large Eddy Simulations (LES) is a balanced choice to explore the physics related to film-cooling. Details of numerical studies on the film cooling by using LES turbulence model is summarized in Table.1.

Guo et al. [24] carried out a numerical study by using large eddy simulations in order to study the effect of blowing ratio and angle of inclination. For the same blowing ratio, it was reported that the counter-rotating vortex shifted to the downstream direction for  $30^\circ$  injection as compared to  $90^\circ$ . Wang et al. [25] carried out large eddy simulations over the film cooling characteristics of the cylindrical and fan-shaped hole in order to understand the vortex structure in the cross flow region. The simulations are performed for two different blowing ratio  $M = 0.5$  and  $M = 1$  and the results suggest that plenty of hairpin vortices are formed in case of fan-shaped hole as compared to the cylindrical hole. Apart from that, time-frequency analysis shows that periodicity in case of fan-shaped hole is weaker than the cylindrical hole. Schiender et al. [26] conducted a numerical study on high-pressure turbine blade trailing edge. The study is carried out by imposing the laminar and turbulent flow conditions in the coolant channel for two different blowing ratio  $M = 0.5$  and  $1.1$ . They reported that at low blowing ratio turbulent coolant flow shows improved film cooling performance over laminar flow, whereas at high blowing ratio opposite phenomena can be observed. Shinn et al. [27] carried out LES study on the flat plate film cooling with the micro-ramp vortex generator. The micro ramp vortex generator was found to create a vortex pair having the opposite sense to the main counter-rotating vortex and thus diminishes the effect of jet lift-off. Eventually, film cooling was found to be better than the configuration without the micro ramp. Renze et al. [28] investigated jet in crossflow using LES. The investigated operating parameters were: density ratio ( $DR = 1.53$ ), blowing ratio ( $M = 1$ ) and free stream Reynolds number ( $Re = 4 \times 10^5$ ). They simulated the

effect of density ratio by using high-density coolant stream of CO<sub>2</sub> and found that flow attachment and recirculation is more sensitive to the velocity ratio as compared to the density ratio. Baagherzadeh [29] carried out numerical analysis with LES in order to predict the behaviour of film cooling under the high blowing ratio. The results of RANS and LES were compared with experimental results. It was concluded that the LES model was in better agreement with experimental results. At high blowing ratio ( $M = 2$ ), where significant jet lift-off is expected, LES predictions were noticeably better than RANS predictions. Gräf et al. [30] used LES study to investigate the compressible flow double row injection compound angle film cooling. The flow study and temperature distributions showed reasonable agreement with the experimental results.

Reverse film cooling holes show a promising design to mitigate the problem of kidney vortices. However, the flow structure related to the reverse cylindrical and shaped holes is not well-understood. To the best of the authors' knowledge, there are lack of experimental data available so far in the literature, on the flow physics of reverse holes. One of the study showed a comparative picture of flow physics of forward and reverse cylindrical holes [20]. In this study, flow physics was explained based on RANS modelling. It is well documented in the literature that RANS is not suitable for predicting the instantaneous flow feature [21,22]. Hence, further exploration of reverse cooling holes is required to understand the flow mechanism and film cooling characteristics of not only cylindrical holes but also shaped holes which are being used extensively.

In the present study, large eddy simulation is carried out to investigate the film cooling performance and flow characteristics of forward-cylindrical (FC) and reverse cylindrical (RC), forward shaped (FS) and reverse shaped (RS) holes. The numerical study is carried with a fixed blowing ratio ( $M = 1$ ), density ratio ( $DR = 2.46$ ) and Reynolds number based on

secondary flow, hole diameter ( $0.9 \times 10^3$ ). The injection of the secondary stream with the main flow has been taken as  $35^\circ$  for both forward and reverse holes.

## 2. Problem description

In order to understand the film cooling characteristics with forward and reverse hole, a numerical investigation has been carried out for cylindrical and shaped holes. The behaviour of film cooling and vortex formation in the flow field has been evaluated by using LES study. Figure 2(a) - (b) show the systematic layout of the computational domains addressed in the present study. In order to protect the surface from the detrimental effect of hot mainstream flow conditions 128 m/s and 1561K, a secondary stream relatively at lower temperature is injected at  $35^\circ$  with different hole configurations viz: (i) Forward cylindrical (FC); (ii) Reverse cylindrical (RC); (iii) Forward shaped (FS); (iv) Reverse shaped (RS). The secondary stream of air is supplied to the hole via the plenum chamber of dimensions  $5D \times 5D \times 5D$ . The film cooling performance is evaluated over the flat surface for the length of  $30D$  where  $D$  is the diameter of the hole, considered as 1 mm [31].

## 3. Computational method

### 3.1 Mathematical Modelling

In case of the Large Eddy Simulations (LES) the governing equations are obtained by following filtering operations:

$$\bar{\varphi}(x'_i, t) = \int_{\Delta} \varphi(x'_i, t) G(|x_i - x'_i|) d\bar{x}_i \quad (1)$$

where the term,  $\bar{\phi}(x'_i, t)$  and  $G$  represents arbitrary resolved quantity and the filter function respectively. In the present study, the top-hat filter is considered as filtering function. The 3D non-uniform grids are used and the filter width,  $\Delta$  is taken as cube root of cell volume as follows [32]:

$$\Delta = (\Delta x \Delta y \Delta z)^{1/3} \quad (2)$$

In order to account the variations in the density with the temperature changes, the Favre Averaging is used as follows:

$$\tilde{\phi}(x'_i, t) = \frac{\overline{\rho \phi(x'_i, t)}}{\bar{\rho}} \quad (3)$$

The instantaneous variable,  $\phi(x'_i, t)$  can be written in terms of resolved and unresolved

$$\phi(x'_i, t) = \tilde{\phi}(x'_i, t) + \phi''(x'_i, t) \quad (4)$$

where the term  $\tilde{\phi}(x'_i, t)$  and  $\phi''(x'_i, t)$  represents the resolved (filtered) and un-resolved (sub grid scale) components respectively.

Flow is assumed to be turbulent and Large eddy simulations (LES) is used for modelling turbulent flow the governing equations, viz. continuity, momentum and energy equations for the flow are given in Eq. 5- 7, as referred in literature [33].

$$\frac{\partial \bar{\rho}}{\partial t} + \frac{\partial \bar{\rho} \tilde{U}_i}{\partial x_i} = 0 \quad (5)$$

$$\frac{\partial \bar{\rho} \tilde{U}_i}{\partial t} + \frac{\partial (\bar{\rho} \tilde{U}_i \tilde{U}_j)}{\partial x_j} = \frac{\partial \bar{p}}{\partial x_i} + \frac{\partial}{\partial x_i} \left[ \mu \left( \frac{\partial \tilde{U}_i}{\partial x_j} + \frac{\partial \tilde{U}_j}{\partial x_i} \right) - \frac{2}{3} \mu \frac{\partial \tilde{U}_k}{\partial x_k} \delta_{ij} \right] + \frac{\partial \bar{A}_{u_i u_j}}{\partial x_i} \quad (6)$$

$$\bar{\rho} C_p \frac{\partial \tilde{T}}{\partial t} + \bar{\rho} C_p \tilde{U}_i \frac{\partial \tilde{T}}{\partial x_i} = \frac{\partial}{\partial x_i} \left( \frac{\mu C_p}{\text{Pr}} \frac{\partial \tilde{T}}{\partial x_i} \right) + \frac{\partial \bar{A}_{u_i T}}{\partial x_i} \quad (7)$$

Here, the term  $U$ ,  $p$ ,  $T$  and  $A$  indicates velocity, pressure, temperature and stress tensor respectively where bar terms,  $\bar{U}$  indicates the resolved (filtered) velocity and tilde over the term,  $\tilde{U}$  indicates Favre averaged quantity. The Favre averaging is used to account the variations in the density with changes in temperature. The density of air is calculated by using the ideal gas equations. The unknown terms like sub-grid stress tensor ( $\bar{A}_{u_i u_j}$ ) and sub-grid scale heat flux ( $\bar{A}_{u_i T}$ ) in Eqs. (6) and (7) respectively, are computed by, sub-grid scale (SGS) model.

The SGS viscosity using eddy viscosity hypothesis can be expressed as,

$$A_{ij} = -2\mu_{SGS}\tilde{S}_{ij} + \frac{2}{3}k_{SGS}\delta_{ij} \quad (8)$$

where,  $\tilde{S}_{ij}$  is called filtered strain rate tensor which is expressed as follows:

$$\tilde{S}_{ij} = \frac{1}{2} \left[ \frac{\partial \tilde{U}_i}{\partial x_j} + \frac{\partial \tilde{U}_j}{\partial x_i} \right] \quad (9)$$

The eddy viscosity term in Eq. (8) can be calculated by using the one equation eddy-viscosity model “as follows [34]:

$$\mu_{SGS} = C_k (k_{SGS})^{1/2} \Delta \quad (10)$$

Where, the turbulent kinetic energy ( $k_{SGS}$ ) can be expressed as, [35]

$$k_{SGS} = \frac{1}{2} (\overline{U_j U_j} - \bar{U}_j \bar{U}_j) \quad (11)$$

The comprehensive LES study suggested that one equation eddy-viscosity model shows a better predictions near the wall hence it is considered for the present study [36]. To compute  $k_{SGS}$ , the present approach (one equation eddy-viscosity model) solves additional transport equation. :

$$\frac{\partial k_{SGS}}{\partial t} + \frac{\partial \tilde{U} k_{SGS}}{\partial x_j} = \frac{\partial}{\partial x_j} \left( \frac{\mu_t}{\sigma_k} \frac{\partial k_{SGS}}{\partial x_j} \right) A_{ij} \frac{\partial \tilde{U}}{\partial x_j} - C_\epsilon \frac{(k_{SGS})^{3/2}}{\Delta} \quad (12)$$

The model constants  $C_k = 0.094$ ,  $C_\varepsilon = 0.916$  and  $\sigma_k = 1.048$ , are taken from reference [37]. The SGS heat flux,  $\bar{A}_{u,T}$  in equation (7) is calculated based on the simple gradient diffusion hypothesis.

$$\bar{A}_{u,T} = \frac{-\mu_{SGS}}{\text{Pr}_t} \frac{\partial \tilde{T}}{\partial x_j} \quad (13)$$

### 3.2 Numerical schemes

In the present numerical study, the large eddy simulations are carried out and the filtered equations of continuity, momentum and energy are solved by finite volume method based CFD source codes (OpenFOAM 5.0 and Greenshields [38]). The convective and diffusive fluxes are calculated by second order accurate central differencing scheme. The temporal term in governing equations discretised by the backward scheme is of second-order accurate. The solution is considered to be converged when the residuals of continuity, velocity, turbulence quantities and energy fall below  $10^{-6}$ . In order to accurately capture the cross flow physics, the time step is selected based on the Courant–Friedrichs–Lewy (CFL) number,  $\text{CFL} = 0.8$  according to the guidelines of Acharya et al.[39]. The PIMPLE algorithm is used for pressure and velocity coupling.

The present numerical simulations are transient by nature, but the quasi-static state reached after 15000 time steps. So, the time averaging is performed for the parameters such as pressure, temperature and velocity. The quasi-static state is referred as condition where statistical differences in the time-averaged quantities are negligible (generally lies in the range of 2-4%). The time averaging is performed over a period after quasi-static condition until the statistical differences in the average quantities fall below acceptable range of (2%), which is further requires 10-15 flow overtime. The flow over time is the time taken by mainstream to reach the outlet.

### 3.3 The Fluid properties

Air is used as a working fluid for both mainstream and the secondary stream. The temperature difference in the region is very large so that the variation in the physical properties of air with temperature is considered in the present study. Air is assumed to be incompressible which means that the density of air depends on the local fluid temperature and operating pressure in the physical domain. A fourth order polynomial as suggested in reference [40], is used for the thermal conductivity, specific heat and dynamic viscosity. All the properties are valid in the temperature range of 100 K - 2300 K. The temperature-dependent properties are given in the Eqs. 14-16.

Specific heat, ( $C_p$ ) J/kg.K

$$C_p = (9.0813 \times 10^{-11})T^4 - (4.8066 \times 10^{-7})T^3 + (8.073 \times 10^{-4})T^2 - 0.32136T + 1.0450 \times 10^3 \quad (14)$$

Dynamic viscosity ( $\mu$ ), Pa.s

$$\mu = (1.7020 \times 10^{-14})T^3 - (4.0405 \times 10^{-11})T^2 + 6.8539 \times 10^{-8}T + 1.0616 \times 10^{-6} \quad (15)$$

Thermal conductivity ( $K_{th}$ ), W/m.K

$$K_{th} = (7.9957 \times 10^{-12})T^3 - (2.4013 \times 10^{-8})T^2 + (8.3047 \times 10^{-5})T + (2.8822 \times 10^{-3}) \quad (16)$$

### 3.4 Boundary conditions and operating parameters

The inlet of the mainstream and plenum is assigned to be time invariant turbulent velocity profile obtained from the RANS study of channel flow (Figs. 2 (a)-(b)). The outlet of the domain is assumed to be pressure exit with zero-gauge pressure. All the input parameters for the different geometrical configurations are given in Table. 2. The side walls in the lateral direction of the mainstream flow of the flow field are considered as the periodic boundary. All other walls in the domain are assigned as the no-slip adiabatic condition. The detailed descriptions of boundary conditions are given in Table.3. The plenum chamber is provided to obtain the actual experimental conditions of coolant supply [41]. All

simulations use mainstream conditions of 128 m/s at 1561 K with the inlet temperature in the plenum specified as 644 K at density ratio (DR) of 2.46. The plenum inlet boundary condition is fixed for blowing ratio ( $M = 1$ ) and secondary flow Reynolds number of  $0.9 \times 10^3$  in coolant pipe.

### 3.5 Grid Resolution

To ensure the computational accuracy in LES, all the computational domains were discretised by structural hexahedral cells as shown in Fig. 3 (a)-(d). The grid used for the numerical study of all four domains shows nearly similar topology, the only number of grid points are slightly different from each other. As the turbulent length scale is highly mesh-sensitive for LES based computation [42,43], a careful design of the computational grid is a prerequisite. The grid is highly refined near the wall regions and secondary flow exit. The minimum size of the grid for all computational domains in the direction normal to the wall is  $5 \times 10^{-6}$  (normalized by  $L_{ref} = 40D$ , where  $D = 10^{-3}$  m). For the present LES study, the grid topology is carefully designed to ensure computational accuracy. The recent LES study of Georgiadis et al. [44] recommends the wall resolved LES rather than the grid convergence study due to the basic nature of LES. However, in our present study, the basic criteria for grid selection is the total number of cells as well as the non-dimensional grid refinement parameters, followed by the previous LES studies which are shown in Table. 4. The mesh is well refined near the walls and critical zones. Therefore, the grid density in the domain is characterized by:  $\Delta x^+ < 60$ ,  $\Delta y^+ < 1$  and  $\Delta z^+ < 60$  where  $\Delta x^+$ ,  $\Delta y^+$  and  $\Delta z^+$  represents the non-dimensional grid spacing near the wall in the direction tangent to the wall, normal to the wall, and spanwise respectively, followed by previous LES[44–49]. The grid resolution near the wall surface for different holes viz: FC, RC, FS and RS can be described in terms of non-dimensional ratios,  $\Delta x/L_{ref} < 0.0017$  and  $\Delta y/L_{ref} < 0.0065$ .

## 4. Results and Discussions

In this section, the analysis of the results of the numerical investigation is presented. The film cooling on the flat surface is reported with four different hole configurations. The numerical analysis is conducted for the fixed angle of injection  $35^\circ$ , blowing ratio;  $M = 1$ , density ratio; and  $DR = 2.46$ . For present investigation well resolved large eddy simulations are conducted and time average results of film cooling effectiveness, non-dimensional velocity magnitude and pressure drop calculations are presented.

#### **4.1 Fluid Flow and Heat Transfer Validations**

The computational results validated with the experimental results from literature [20]. For effectiveness validations the operating parameters viz.  $M = 1$  and  $DR = 0.91$  are considered which is same as experimental conditions of reference [20]. For this validation, one might expect film heating instead of film cooling because,  $DR < 1$ . For the flat plate film cooling, it has been shown that at low-density ratio film heating is analogous to film cooling [40]. The centreline and lateral average effectiveness of forward and reverse hole are compared with reference data. Figure 4(a) shows that the centreline effectiveness of forward cylindrical hole is in close agreement with the experimental data. From Fig. 4 (b), it can be seen that the lateral average film cooling effectiveness has small deviations near the downstream of the coolant hole. The centre line effectiveness and lateral average effectiveness of reverse hole given in Figs. 4 (c-d) showed excellent agreement near the hole. However, a small deviation can be observed at downstream of the hole. The present computational model follows the nature of variations shown in the experimental data; however, the film cooling effectiveness is slightly over-predicted.

#### **4.2 Film Cooling Effectiveness: Centreline and Lateral Average**

In order to compare the centreline film cooling effectiveness for various hole configurations, the effectiveness is plotted along the centreline ( $Z/D = 0$ ) over the flat surface as shown in Fig. 5(a). It

can be observed from Fig. 5(a) that the centreline effectiveness of FC and FS holes are much higher than that of RC and RS holes along the downstream (i.e.  $X/D$ ). It can also be inferred that FC hole is more effective along the centreline than FS hole for a short distance in the downstream of the hole, i.e.  $X/D = 8$ . From  $X/D = 8$  to 30, FS hole effectiveness is maximum among all hole configurations. The centreline effectiveness of FC is relatively higher at a very short distance in the downstream of the hole due to more coolant skewness toward the narrow central part of the surface. Lateral average film cooling effectiveness would be a better representation for performance assessment of these cooling holes. Figure 5(b) and (c) shows the variations of lateral average effectiveness of various hole configurations for both cylindrical and shaped holes. The lateral average is obtained from the downstream edge of the hole (where no-hole footprints are presents). It may be emphasized that the width of the shaped hole is  $6D$  due to its lateral expansion (more than  $3D$  in the lateral direction). As the domain width is different for both cylindrical and shaped holes, the lateral average effectiveness is compared separately in Fig. 5 (b) and Fig. 5 (c). For the FC and RC lateral averaging is taken over lateral distance,  $Z/D = -1.5$  to  $1.5$ . In case of shaped holes, FS and RS the lateral averaging is taken over the  $Z/D = -3$  to  $3$ . It is considered to a most important effectiveness parameter in film cooling which represents the spread of coolant stream at each lateral location, downstream of the injection holes. Figure 5 (b) clearly shows that the lateral average effectiveness of RC is higher than FC, for all locations along with the flow. The effectiveness of RC is 1.9 times the RC near the hole at  $X/D = 1$ . However, in Fig. 5 (c), RSH shows better lateral average effectiveness as compared to FSH near the hole from  $X/D = 0$  to 10 and in the near the hole region ( $X/D = 1$ ), the effectiveness is 1.5 times the FS. The effectiveness contours in Figs. 6 (a)-(d), reflects that the coolant coverage is better in case of reverse holes than the forward hole, which essentially means better lateral average effectiveness. Apart from these observations, Figure 5 (c), reveals that the RS is 1.5 to 1.17 times more effective than FS at  $X/D = 1$  and  $X/D = 30$  respectively. The relative improvement in the lateral average effectiveness is maximum for RS hole among shown hole shapes.

Figures 7-10 show the streamlines contours of non-dimensional temperature, theta ( $\theta$ ). The formation of vortex pair in case of film cooling flows plays a vital role in the mixing of coolant with

the mainstream and coolant jet lift-off that finally governs the film cooling performance. It has been seen that as coolant/secondary jet exit from the simple cylindrical hole into the cross flow region and split into counter-rotating pairs (CRVP) which is of similar evidence from literature [2]. In this study four different planes are considered for the systematic understating of formation of CRVP. Figure 7(a) shows the flow streamlines for the FC hole, in the X-Z plane at  $Y/D = 0$ . The streamlines near the flat surface at  $Y/D = 0$ , is presented by taking a plane one node above the surface. The streamlines for the FC holes appear to be symmetric and skewed towards the centreline. As a result of this fact, most of cooling effects can be seen along a narrow part of the central region. At  $X/D = 1$ , the formation of kidney vortices in the plane Y-Z i.e. normal to the flow leads to “coolant stream lift off” through mutual induction as shown in Fig. 7 (b). As the flow moves in the downstream direction (Fig. 7-c) at  $X/D = 3$  in Y-Z plane, the strength of CRVP increases that leads to coolant lift-off. In Fig. 6 (d) at  $Y/D = 0.5$  in X-Z plane, some cooling effect can be observed that actually represents that coolant is not trapped below this plane and hence the coolant coverage over the surface is lower. The present observation of counter-rotating vortex pairs for FC holes shows close consistency with the previous studies [2].

Figure 8(a) illustrates the three-dimensional vortex pair formation for the RC. This figure distinctly shows a vortex pair in the plane parallel to mainstream flow which promotes the coolant spread in the lateral direction. The vortex pair shown in Fig 8(a) is distinctly different from the commonly observed CRVP. Referring the co-ordinate sign convention in the present study, CRVP appears in Y-Z plane downstream of hole whereas vortices formed in case of the reverse hole are predominately in X-Z plane. The other difference in these two vortices is: CRVP has a sense of upward movement which enhances mixing with the mainstream whereas vortices observed in the case of reverse holes directs fluid in the lateral direction. This results in uniform spreading of the coolant onto the hot surface which eventually will diminish thermal stresses. Figure 8 (b) shows the formation vortex pair for the RC in the plane of a flat surface (X-Z plane) at  $Y/D = 0$ . It can be observed from this figure that the vortices in the X-Z plane are extended to  $X/D = 4$  downstream of the hole for the investigated flow conditions. The temperature of the coolant suggests that coolant is not mixed with the mainstream up to  $X/D = 4$  and hence higher area weighted average film cooling effectiveness is observed. Since, the

vortices observed in Fig. 8(a) are three dimensional in nature, the analysis on Y-Z plane can shed some light on the propagation of these vortices. Figure 8 (c-d) shows the vortices in the Y-Z plane at  $X/D = 1$  and  $X/D = 3$ , respectively. It can be observed from Fig. 8 (c) that the coolant penetrates into mainstream up to  $Y/D = 0.4$  at  $X/D = 1$ , just after the injection. Despite the counter-rotating vortices, coolant remains confined to  $Y/D = 0.4$  as downstream distance increases to  $X/D = 3$ , depicted in Fig. 8 (d). This also indicates that the vortices observed in case of reverse holes are not having any sense of upward movement. Figure 8 (e) shows streamlines plot X-Z plane parallel to the flat surface at  $Y/D = 0.5$ . The plane reveals that the streamlines are more uniform and coolant effect can be observed. This confirms that coolant is not mixed with the mainstream and provides an adequate blanket to the heated surface eventually enhancing the cooling effectiveness.

In the case of shaped holes, the observations are different from the conventional cylindrical holes. Figure 9 (a) represents streamlines for the FS hole at  $Y/D = 0$  in X-Z plane, that shows a uniform pattern of flow streamlines without any skewness. However, a counter-rotating pair can be seen at  $X/D = 2$  in Y-Z plane, as shown in Fig. 9 (b) which further transform into a kidney vortex accompanied by anti-kidney pair at  $X/D = 5$  as shown in the Fig. 9 (c). As a result of strong anti-kidney pair in Fig. 9 (b), the tendency of coolant jet lift-off dominates. Thus, a better coolant coverage is observed in Fig. 6 (a)-(c) for FS as compared to FC hole. The present observations of FS show consistency with previous experimental results from reference [9]. Despite the presence of anti-kidney vortices which are suppressing the upward movement of the coolant, Fig. 9 (d) shows that there is an only a small amount of coolant at  $Y/D = 0.5$ . Similar to the reverse cylindrical hole, a three-dimensional vortex predominately in the X-Z plane is observed as depicted in Fig. 10 (a) and the formation vortex pair for the RS in the plane of a flat surface (Z-X plane) at  $Y/D = 0$ , is shown in Fig. 10 (b). It can be observed that the penetration of the coolant into the mainstream at the location of injection is up to  $Y/D = 0.6$  which is not significantly increased as downstream distance increases (Fig. 10-d). Rather, the lateral spread of the coolant increases with the increase in downstream distance. These vortices show similarity with the vortex pair discussed for the RC hole in the previous section (Figs. 8a – b). It is also observed from Fig. 10 (b)-(c) as the jet moves downstream from  $X/D = 2$  to 5, the strength of counter-rotating

vortex reduces and hence the jet lift-off also diminishes. Figure 10 (e) shows a plane parallel to the plane shown in Fig. 10 (a), where more regular streamline with uniform coolant spread can be observed.

### 4.3 Local lateral Effectiveness

The variations in local lateral film cooling effectiveness for various hole configurations are shown in Fig. 11. The different holes are compared for stream-wise distance  $X/D = 5$  and  $10$ . From Fig. 11 (a)-(b), it can be observed that for the FC, the local effectiveness is relatively higher in the central region as compared to RC. This is because of the more skewed flow of coolant along the central line. Apart from this fact, FC coolant spread in the lateral direction is poor which results in a lower effectiveness and hence increased temperature (Figs. 6 (a) and (b)). However, the coolant coverage for RC much better than that of FC, which leads to uniform effectiveness throughout the lateral directions of  $Z/D$  from  $-1.5$  to  $1.5$  as shown in Fig. 11 (a)-(b).

A similar observation is reported with FS in Fig. 11(c)-(d), where the coolant coverage is much limited to the width of the hole in the central region at  $Z/D = 0$ , which leads lower effectiveness in the lateral directions of  $Z/D$  from  $-3$  to  $3$ , for  $X/D = 5$  and  $10$ . Most of the coolant spread in the lateral direction is limited to  $Z/D = -1$  to  $1$  and beyond this region, the coolant spread is poor which results in a faster decay of lateral effectiveness for FS. As compared to FS the lateral effectiveness of RS is much higher and coolant spread is almost uniform in the lateral directions of  $Z/D$  from  $-2$  to  $2$ . This phenomenon is clearly seen from contours results for FS and RS in Fig. 6 (c) and (d). The FS coolant spread in the lateral direction is limited to the width of injection holes whereas in case of RS, coolant spreading is almost double of the width of the injection hole.

### 4.4 Flow velocity profiles

The flow characteristics near the secondary flow exit are shown in the Fig.13. The present results for non-dimensional velocity magnitude compared with the experimental measurement

[28] using particle image velocimetry (PIV). The available experimental data of PIV at  $VR = 0.28$ ,  $M = 0.5$  and  $DR = 1.53$  are compared with the present numerical model at  $VR = 0.46$ ,  $M = 1$  and  $DR = 2.46$ . Figure 12 shows the non-dimensional mean velocity magnitude for different hole configurations such as FC, RC, FS and RS hole. The velocity profiles are plotted along  $Y/D$  for centreline locations at  $X/D = 0, 1, 1.5$  and  $2$ . All the velocity profiles look nearly similar outside the shear layer. However, the differences can be seen at the inner part of shear layer i.e. vicinity of cooling surface. The velocity gradients of FC and FS holes are steeper as compared to RC and RS holes for the investigated stream wise locations ( i.e.  $X/D = 0$  to  $2$ ). The steeper velocity profile for RC and RS holes shows higher turbulence due to its opposite flow to the mainstream. It may be inferred that the discharge coefficient is strongly influenced by injection configuration. The discharge coefficient is inversely proportional to the pressure drop in coolant hole. The pressure losses are higher in reverse injection configurations resulting reduction in discharge coefficient as shown in Fig. 13. Also, it will have more aerodynamic loss on the main stream flow. The results show that the qualitative trend of non-dimensional velocity follows the trend predicted by the experimental findings [28].

#### **4.5 Discharge Coefficient**

Discharge Coefficient ( $C_d$ ) is an important parameter to express the pressure losses through coolant injection holes. In the previous sections it has been seen that the RC and RS holes, film cooling performance found to be better than FC and RC holes (Fig. 6-b). However, one might expect higher pressure losses in case of reverse injection holes, since the flow of coolant is opposite to the mainstream. In this section, discharge coefficient is plotted for all four hole configurations viz. FC, RC, FS and RS for comparison of the pressure losses. The discharge coefficient ( $C_d$ ) is defined as the ratio of the actual mass flow rate to the theoretical mass flow

rate in the coolant holes. The theoretical mass flow rate is calculated by using Eq. (17), assuming one directional isentropic expansion from coolant total pressure ( $P_{tc}$ ) at the inlet to the cooling hole to the mainstream static pressure ( $P_{ms}$ ) as followed in reference [20].

$$m_{theoretical} = A_{cs} P_{tc} \left( \frac{P_{ms}}{P_{tc}} \right)^{\gamma+1/2\gamma} \sqrt{\frac{2\gamma}{(\gamma-1)RT_{tc}} \left[ \left( \frac{P_{tc}}{P_{ms}} \right)^{\gamma-1/\gamma} - 1 \right]} \quad (17)$$

Here,  $\gamma$  is the ratio of specific heats,  $R$  is gas constant,  $T_{tc}$  is coolant total temperature and  $A_c$  is the cross-sectional area of the cooling hole. For the FC and RC hole, the cross-sectional area remains same throughout however for shaped holes viz. FS and RS, it changes from cylindrical inlet to expanded exit. In order to calculate the theoretical mass flow rate for shaped holes with expanded exit, it was suggested to consider the cross-section of the inlet of injection holes[50]. Thus, the discharge coefficient of shaped holes can be directly compared with the cylindrical holes. This is actually the slight deviation from the actual calculation however it makes contouring of shaped holes more convenient. The total pressure from reference [51], is taken at the inlet of the hole near the plenum and mainstream static pressure is taken at  $X/D = -5$  (means upstream of injection holes).

Figure 13 shows the systematic comparison of the coefficient of discharge for different hole configurations. The coefficient of discharge of FC at  $35^\circ$  injection angle is compared with forward cylindrical hole results from literature [20], at  $30^\circ$  for blowing ratio ( $M$ ) =1. It found to be 18.1% higher than the present results. This deviation may be attributed to being the difference in density ratio (DR) and mainstream Reynolds number (Re) and length to diameter ratio (L/D). However, the coefficient of discharge for RC at  $35^\circ$  injection angle and blowing ratio ( $M$ ) =1 shows excellent agreement with reverse cylindrical hole, from literature findings [18, 20]. The FS hole discharge coefficient at  $35^\circ$  injection angle and blowing ratio ( $M$ ) = 1

also shows good agreement with results of Liu et al. [52] at 30° injection angle and blowing ratio ( $M$ ) = 1. Figure 13 also illustrates that the discharge coefficients of FC hole are 10% more compared to RC hole. The discharge coefficient of FS hole is 3.7 % more than that of RS hole. It is also important to observe from the figure that the discharge coefficient of FS is 9.6 % more than the FC hole and discharge coefficient of RS is 16.67% more than RC hole. In parallel injection (0° angle of incidence), the discharge coefficient is noted as 0.72 as cited in reference [39].

The discharge coefficient is inversely related to pressure loss. It is interesting to note that the use of reverse shaped holes increases film cooling effectiveness by 70 to 300 % (from coolant injection hole to rear end of target surface) at the 4% addition pumping power as compared to the forward shaped holes. The improved spread of coolant and increased effectiveness can further decrease the total mass of coolant required to meet the targeted temperature. Hence, overall pumping power required may decrease in actual operation where a large number of cooling holes are made on the surface. From the Fig. 13, it can also be observed that the discharge coefficient is strongly influenced by injection configuration. In case of reverse holes the discharge coefficient are lower as compared to forward holes. The discharge coefficient is inversely proportional to the pressure drop in coolant hole. Hence, it can be observed that pressure losses are more in reverse injection configurations.

Figure 14 shows the contours of velocity magnitude non-dimensionalized at the exit of the coolant hole for all the four injection configurations. The non-dimensional velocity ( $U/U_{ms}$ ), contour is plotted by taking a plane one node below the flat surface. Figure 14 shows the shifting of velocity profile towards the trailing edge in case of reverse hole. It can be observed from Fig. 14 that for the RC and RS velocity magnitude near the leading edge is much lower as compared to trailing edge. The coolant flow is in the opposite direction to mainstream

hence the hole is partially blocked in upstream (leading side). The opposite flow of coolant stream also results in greater momentum loss. The partial blockage adds resistance to the flow and thus it requires more pumping power. Apart from the forward injection cases such as FC and FS holes, the velocity distribution found to be nearly uniform throughout the hole. Similar, results were also reported from reference [20].

## 5. Conclusions

Large eddy simulation is conducted in order to study the effect cylindrical and shaped hole configuration over the forward and reverse injection film cooling performance. This study is carried for a flat surface for the different hole configurations. The other operating parameters are, blowing ratio ( $M$ ) = 1,  $DR = 2.46$  and  $35^\circ$  injection angle. Based on the present study following inferences can be drawn: -

1. The vortices observed in the case of reverse cylindrical and reverse shaped are predominately in the plane of the plate and mitigate the problem of formation of kidney vortices.
2. The reverse cylindrical (RC) hole shows better laterally average effectiveness over the forward cylindrical (FC) hole. The maximum improvement in lateral average effectiveness lies in the range of 33-100%, from downstream to hole exit. The coolant coverage in case of reverse injection is nearly uniform throughout the surface.
3. The coolant coverage of reverse shaped (RS) hole much better and covers more area as compared to the forward shaped (FS) hole. Improvement in lateral average effectiveness of RS hole is maximum near the hole which is 50% more compared to the RC hole. Apart from this fact, the coolant coverage for RS is more uniform as compared to FS.

4. The maximum lateral average effectiveness is obtained with RS among all four considered injection configurations.
5. The pressure drop is maximum for RC and minimum for FC. Moreover, the pressure drop in case of RS is comparable to that of FS hole.

## Acknowledgement

Authors are thankful to the department of science and technology (SERB), New Delhi under early career research award; project ref. No. ECR/2016/001364; for the computational facility to carry out the numerical study in the Department of Mechanical Engineering at NIT Manipur, Manipur, India.

## Reference

- [1] Goldstein, R. J., Eckert, E. R. G., and Burggraf, F., 1974, "Effects of Hole Geometry and Density on Three-Dimensional Film Cooling," *Int J Heat Mass Transf*, **17**(5), pp. 595–607.
- [2] Fric, T. F., and Roshko, A., 1994, "Vortical Structure in the Wake of a Transverse Jet," *J Fluid Mech*, **279**, pp. 1–47.
- [3] Kelso, R. M., Lim, T. T., and Perry, A. E., 1996, "An Experimental Study of Round Jets in Cross-Flow," *J Fluid Mech*, **306**, pp. 111–144.
- [4] Smith, S. H., and Mungal, M. G., 1998, "Mixing, Structure and Scaling of the Jet in Crossflow," *J Fluid Mech*, **357**, pp. 83–122.
- [5] Goldstein, R. J., Eckert, E. R. G., and Ramsey, J. W., 1968, "Film Cooling with Injection through Holes: Adiabatic Wall Temperatures Downstream of a Circular Hole," *J Eng Gas Turbines Power*, **90**(4), pp. 384–393.

- [6] Andreopoulos, J., 1985, "On the Structure of Jets in a Crossflow," *J Fluid Mech*, **157**, pp. 163–197.
- [7] Shvarts, A. G., and Yastrebov, V. A., 2018, "Fluid Flow across a Wavy Channel Brought in Contact," *Tribol Int*, **126**, pp. 116–126.
- [8] Renze, P., Schröder, W., and Meinke, M., 2008, "Large-Eddy Simulation of Film Cooling Flows at Density Gradients," *Int J Heat Fluid Flow*, **29**(1), pp. 18–34.
- [9] Haven, B. A., and Kurosaka, M., 1997, "Kidney and Anti-Kidney Vortices in Crossflow Jets," *J Fluid Mech*, **352**, pp. 27–64.
- [10] Rozati, A., and Tafti, D. K., 2008, "Large Eddy Simulation of Leading Edge Film Cooling - Part II: Heat Transfer and Effect of Blowing Ratio," *J Turbomach*, **130**(4), pp. 1–7.
- [11] Zheng, Y., and Hassan, I., 2014, "Experimental Flow Field Investigations of a Film Cooling Hole Featuring an Orifice," *Appl Therm Eng*, **62**(2), pp. 766–776.
- [12] Saumweber, C., Schulz, A., and Wittig, S., 2003, "Free-Stream Turbulence Effects on Film Cooling with Shaped Holes," *J Turbomach*, **125**(1), pp. 65–73.
- [13] Thole, K., Gritsch, M., Schulz, A., and Wittig, S., 1996, "Flowfield Measurements for Film-Cooling Holes with Expanded Exits," *ASME 1996 Int Gas Turbine Aeroengine Congr Exhib GT 1996*, **4**(April 1998), pp. 327–336.
- [14] Bell, C. M., Hamakawa, H., and Ligrani, P. M., 2000, "Film Cooling from Shaped Holes," *J Heat Transfer*, **122**(2), pp. 224–232.
- [15] Dhungel, A., Lu, Y., Phillips, W., Ekkad, S. V., and Heidmann, J., 2009, "Film Cooling from a Row of Holes Supplemented with Antivortex Holes," *J Turbomach*, **131**(2), pp. 1–10.
- [16] Ely, M. J., and Jubran, B. A., 2009, "A Numerical Evaluation on the Effect of Sister Holes on Film Cooling Effectiveness and the Surrounding Flow Field," *Heat Mass*

- Transf und Stoffuebertragung, **45**(11), pp. 1435–1446.
- [17] Wu, H., Cheng, H., Li, Y., Rong, C., and Ding, S., 2016, “Effects of Side Hole Position and Blowing Ratio on Sister Hole Film Cooling Performance in a Flat Plate,” *Appl Therm Eng*, **93**, pp. 718–730.
- [18] Shetty, S., Li, X., and Subbuswamy, G., 2012, “Ht2012-58 Numerical Simulation on Gas Turbine Film Cooling of Curved Surface,” pp. 1–8.
- [19] Chen, A. F., Li, S. J., and Han, J. C., 2015, “Film Cooling for Cylindrical and Fan-Shaped Holes Using Pressure-Sensitive Paint Measurement Technique,” *J Thermophys Heat Transf*, **29**(4), pp. 775–784.
- [20] Singh, K., Premachandran, B., and Ravi, M. R., 2017, “Experimental and Numerical Studies on Film Cooling with Reverse/Backward Coolant Injection,” *Int J Therm Sci*, **111**, pp. 390–408.
- [21] Tyagi, M., and Acharya, S., 2003, “Large Eddy Simulation of Film Cooling Flow from an Inclined Cylindrical Jet,” *J Turbomach*, **125**(4), pp. 734–742.
- [22] ACHARYA, S., TYAGI, M., and HODA, A., 2006, “Flow and Heat Transfer Predictions for Film Cooling,” *Ann N Y Acad Sci*, **934**(1), pp. 110–125.
- [23] Tyliszczak, A., 2008, “Notations C,” pp. 243–256.
- [24] Guo, X., Schröder, W., and Meinke, M., 2006, “Large-Eddy Simulations of Film Cooling Flows,” *Comput Fluids*, **35**(6), pp. 587–606.
- [25] Ke, Z., and Wang, J., 2016, “Conjugate Heat Transfer Simulations of Pulsed Film Cooling on an Entire Turbine Vane,” *Appl Therm Eng*, **109**, pp. 600–609.
- [26] Schneider, H., von Terzi, D., and Bauer, H. J., 2010, “Large-Eddy Simulations of Trailing-Edge Cutback Film Cooling at Low Blowing Ratio,” *Int J Heat Fluid Flow*, **31**(5), pp. 767–775.
- [27] Shinn, A. F., 2017, “IMECE2011-6 5267.”

- [28] Renze, P., Schröder, W., and Meinke, M., 2008, “Large-Eddy Simulation of Film Cooling Flows with Variable Density Jets,” *Flow, Turbul Combust*, **80**(1), pp. 119–132.
- [29] Baagherzadeh Hushmandi, N., 2018, “Large Eddy Simulation of Flat Plate Film Cooling at High Blowing Ratio Using Open FOAM,” *Heat Mass Transf und Stoffuebertragung*, **54**(6), pp. 1603–1611.
- [30] Gräf, L., and Kleiser, L., 2011, “Large-Eddy Simulation of Double-Row Compound-Angle Film Cooling: Setup and Validation,” *Comput Fluids*, **43**(1), pp. 58–67.
- [31] Wang, T., and Li, X., 2008, “Mist Film Cooling Simulation at Gas Turbine Operating Conditions,” *Int J Heat Mass Transf*, **51**(21–22), pp. 5305–5317.
- [32] Schumann, U., 1975, “Subgrid Scale Model for Finite Difference Simulations of Turbulent Flows in Plane Channels and Annuli,” *J Comput Phys*, **18**(4), pp. 376–404.
- [33] Najm, H. N., Wyckoff, P. S., and Knio, O. M., 1998, “A Semi-Implicit Numerical Scheme for Reacting Flow: I. Stiff Chemistry,” *J Comput Phys*, **143**(2), pp. 381–402.
- [34] Yoshizawa, A., 1986, “Statistical Theory for Compressible Turbulent Shear Flows, with the Application to Subgrid Modeling.,” *Phys. Fluids*, **29**(7, Jul. 1986), pp. 2152–2164.
- [35] Lee, C. Y., and Cant, S., 2017, “Assessment of LES Subgrid-Scale Models and Investigation of Hydrodynamic Behaviour for an Axisymmetrical Bluff Body Flow,” *Flow, Turbul Combust*, **98**(1), pp. 155–176.
- [36] Penttinen, O., 2011, “A PimpleFoam Tutorial for Channel Flow, with Respect to Different LES Models.,” *Change*, pp. 1–23.
- [37] Chang, K. C., and Lee, K. H., 2017, “Determination of Mixing Length in Turbulent Mixing Layer on Basis of Vorticity Field,” *Int J Heat Fluid Flow*, **66**, pp. 121–126.
- [38] OpenFOAM foundation, 2015, “UserGuide OpenFoam,” (December), pp. U129–U165.
- [39] Acharya, S., and Leedom, D. H., 2013, “Large Eddy Simulations of Discrete Hole Film Cooling with Plenum Inflow Orientation Effects,” *J Heat Transfer*, **135**(1).

- [40] Singh, K., Premachandran, B., and Ravi, M. R., 2015, “A Numerical Study on the 2D Film Cooling of a Flat Surface,” *Numer Heat Transf Part A Appl*, **67**(6), pp. 673–695.
- [41] Prenter, R., Hossain, M. A., Agricola, L., Ameri, A., and Bons, J. P., 2017, “Experimental Characterization of Reverse-Oriented Film Cooling,” *Proc ASME Turbo Expo*, **5C-2017**, pp. 1–14.
- [42] Davidson, L., 2009, “Large Eddy Simulations: How to Evaluate Resolution,” *Int J Heat Fluid Flow*, **30**(5), pp. 1016–1025.
- [43] Pope, S. B., 2004, “Ten Questions Concerning the Large-Eddy Simulation of Turbulent Flows,” *New J Phys*, **6**.
- [44] Georgiadis, N. J., Fureby, C., and Defence, S., 2010, “Large-Eddy Simulation : Current Capabilities , Recommended Practices , and Large-Eddy Simulation : Current Capabilities , Recommended Practices , and Future Research,” (November 2014).
- [45] Jiang, Y., Mao, M. L., Deng, X. G., and Liu, H. Y., 2015, “Numerical Investigation on Body-Wake Flow Interaction over Rod-Airfoil Configuration,” *J Fluid Mech*, **779**, pp. 1–35.
- [46] Sakai, E., Takahashi, T., and Watanabe, H., 2014, “Large-Eddy Simulation of an Inclined Round Jet Issuing into a Crossflow,” *Int J Heat Mass Transf*, **69**, pp. 300–311.
- [47] Johnson, P. L., 2012, “Large Eddy Simulation of a Film Cooling Flow Injected From an Inclined Discrete Cylindrical Hole Into a Crossflow With Zero-Pressure Gradient Turbulent Boundary Layer,” (August).
- [48] Pachpute, S., and Premachandran, B., 2018, “Experimental Investigation and Large Eddy Simulations of Turbulent Slot Jet Impingement Cooling of a Circular Cylinder with and without a Quadrilateral Confinement,” *Appl Therm Eng*, **144**, pp. 854–876.
- [49] Babu, H., and Sarkar, S., 2014, “Large Eddy Simulation on the Interactions of Wake and Film-Cooling near a Leading Edge,” *Proc ASME Turbo Expo*, **2D**, pp. 1–14.

- [50] Gritsch, M., Schulz, A., and Wittig, S., 1997, “Discharge Coefficient Measurements of Film-Cooling Holes with Expanded Exits,” Proc ASME Turbo Expo, **3**(97), pp. 557–563.
- [51] Taslim, M., and Ugarte, S., 2004, “Discharge Coefficient Measurements for Flow Through Compound-Angle Conical Holes with Cross-Flow,” Int J Rotating Mach, **10**(2), pp. 145–153.
- [52] Liu, C. L., Liu, J. L., Zhu, H. R., Wu, A. S., He, Y. H., and Zhou, Z. X., 2015, “Film Cooling Sensitivity of Laidback Fanshape Holes to Variations in Exit Configuration and Mainstream Turbulence Intensity,” Int J Heat Mass Transf, **89**, pp. 1141–1154.

## Nomenclature

$A_{ij}$	strain rate, $s^{-1}$
$A_{cs}$	cross-sectional area of coolant hole, $m^2$
$a$	thermal diffusivity
$C_p$	specific heat, KJ/Kg-K
$D$	diameter of cylindrical hole, m
$D_{ms}$	Characteristic length of mainstream inlet, m
$h$	enthalpy, KJ/kg
$K_{th}$	thermal conductivity, W/m-K
$L$	length of hole, m
$T$	Temperature, K
$L_{ref}$	Reference length, m
$M$	blowing ratio, $(\rho U)_{sec}/(\rho U)_{ms}$
$m_{theoretical}$	theoretical mass flow rate through coolant hole, kg/s

$M_a$	Mach number
$P$	pressure, N/m <sup>2</sup>
$p_{ms}$	mainstream static pressure, N/m <sup>2</sup>
$P_{tc}$	coolant total pressure, N/m <sup>2</sup>
$Pr_t$	turbulent Prandtl number
$Pr$	Prandtl number
$R$	gas constant, KJ/kg-K
$Re_{sec}$	secondary stream Reynolds number, $\frac{\rho V_{sec} D}{\mu}$
$S$	rate of strain tensor
$t$	time, s
$\Delta t$	physical time step, s
$T$	Local temperature, K
$T_w$	Wall temperature, K
$T_{tc}$	coolant total temperature, K
$U$	velocity of mainstream, m/s
$U_x, U_y, U_z$	velocity in x,y and z direction, m/s
$U_\tau$	Friction/shear velocity, $\sqrt{\tau/\rho}$
$\Delta x, \Delta y, \Delta z$	grid size in x ,y and z direction respectively, m
$\Delta x^+, \Delta y^+, \Delta z^+$	Non-dimensional grid spacing ( $\frac{\Delta x U_\tau}{\nu}$ , $\frac{\Delta y U_\tau}{\nu}$ and $\frac{\Delta z U_\tau}{\nu}$ respectively)
$X, Y \text{ and } Z$	Coordinate in x, y and z direction.

## Subscripts

<i>ad</i>	adiabatic
<i>abm.</i>	ambient
<i>ms</i>	mainstream
<i>min</i>	minimum
<i>max</i>	maximum
<i>ref</i>	reference
<i>sec.</i>	secondary
<i>SGS</i>	Sub grid scale

## Greek Symbol

$\alpha$	angle of inclination with mainstream,
$\beta$	angle of expansion in stream wise
$\gamma$	angle of expansion in span wise
$\Delta$	cut-off width, m
$\varepsilon$	Effectiveness, $\frac{T_{ms} - T_w}{T_{ms} - T_{Sec}}$
$\theta$	non-dimensional temperature, theta $\theta = \frac{T_{ms} - T}{T_{ms} - T_{Sec}}$
$^\circ$	degree
$\rho$	density of air, kg/m <sup>3</sup>

## Acronyms

CFD	Computational fluid dynamics
-----	------------------------------

CFL	Courant–Friedrichs–Lewy number
CRVP	Counter rotating vortex pair.
DR	Density ratio
FC	Forward cylindrical
FS	Forward shaped
LES	large eddy simulations
PIV	Particle image velocimetry
RANS	Reynolds average Navier stokes equations
RC	Reverse cylindrical
RS	Reverse shaped
SGS	Sub-grid scale
VR	Velocity ratio

### **List of Tables**

Table – 1	Summary of LES studies of film cooling.
Table – 2	Operating parameters considered in the present numerical study.
Table – 3	Boundary conditions considered in the present numerical study.
Table – 4	The comparison of present non-dimensional grid refinement parameters with the recent LES studies.

## List of Figures

Fig. 1	Schematic diagram of film cooling flow with a cylindrical hole [5].
Fig. 2	Three-dimensional domain of film cooling over the flat surface along with boundary conditions: (a) Forward and reverse cylindrical hole; (b) Forward and reverse shaped hole.
Fig. 3	Typical mesh for 3D computational domain: (a) Forward cylindrical hole (FCH); (b) Reverse hole (RCH); (c) Forward shaped hole (FSH); (d) Reverse shaped hole (RCH)
Fig. 4	Comparison of the present numerical result of effectiveness with the experimental results of Singh et al. [20].
Fig. 5	Effectiveness plot for various hole configurations: (a) Centreline effectiveness; (b) Lateral average effectiveness (cylindrical holes); (c) Lateral average effectiveness (shaped holes).
Fig. 6	Effectiveness contours of various hole configurations: (a) Effectiveness contour (FCH); (b) Effectiveness contour (RCH); (c) Effectiveness contour (FSH); (d) Effectiveness contour (RSH).
Fig. 7	Streamline contours of non-dimensional temperature ( $\theta$ ) for FCH: (a) $Y/D = 0$ , (X-Z plane); (b) $X/D = 1$ , (Y-Z plane); (c) $X/D = 3$ , (Y-Z plane); (d) $Y/D = 0.5$ , (X-Z plane).
Fig. 8	Streamline contours of non-dimensional temperature ( $\theta$ ) for RCH at Streamline contours of non-dimensional temperature ( $\theta$ ) for FCH: (a) Three dimensional vortices; (b) $Y/D = 0$ , (X-Z plane); (c) $X/D = 1$ , (Y-Z plane); (d) $X/D = 3$ , (Y-Z plane); (e) $Y/D = 0.5$ , (X-Z plane).
Fig. 9	Streamline contours of non-dimensional temperature ( $\theta$ ) for FSH: (a) Streamline contours of non-dimensional temperature ( $\theta$ ) for FCH: (a) $Y/D = 0$ , (X-Z plane); (b) $X/D = 2$ , (Y-Z plane); (c) $X/D = 5$ , (Y-Z plane); (d) $Y/D = 0.5$ , (X-Z plane).
Fig. 10	Streamline contours of non-dimensional temperature ( $\theta$ ) for RSH and FCH: (a) Three-dimensional vortices; (b) $Y/D = 0$ , (X-Z plane); (c) $X/D = 2$ , (Y-Z plane); (d) $X/D = 5$ , (Y-Z plane); (e) $Y/D = 0.5$ , (X-Z plane).
Fig. 11	Local lateral effectiveness contours: (a) FCH and RCH at $X/D = 5$ ; (b) FCH and RCH at $X/D = 10$ ; (c) FSH and RSH at $X/D = 5$ ; (d) FSH and RSH at $X/D = 10$ .
Fig. 12	Comparison of non-dimensional velocity profiles of various hole configuration at centreline along the Y/D direction at various stream wise locations ( $X/D = 0, 1, 1.5, 2$ ) with PIV results from reference [28].
Fig. 13	Comparison of discharge coefficient ( $C_d$ ) of various hole configurations.
Fig. 14	Non-dimensional velocity contours at flow exit from hole for various hole configurations: (a) FCH; (b) RCH; (c) FSH; (d) RSH.

**Table – 1** Summary of LES studies of film cooling.

Author	Hole Shape	Geometric parameter's	Surface	Operating parameter's	Remarks
Tyagi et al. [21]	Circular	$\alpha = 35^\circ$	flat	M =0.5 and 1 $Re_{ms} = 11000$	The coherent hairpin vortex generation 3D unsteady flow field is investigated.
Acharya et al. [22]	Circular	$\alpha = 35^\circ$	flat	M =0.5 to 2 DR = 2	Longer delivery tube shows higher effectiveness
Gauo et al. [24]	Circular	$\alpha = 30^\circ$ & $90^\circ$	flat	--	Formation of kidney vortex
Wang et al.[25]	Fan shaped and circular	$\alpha = 35^\circ$	flat	M = 0.5 and 2	Investigation of voratical structure with blowing ratio.
Schiender et al.[26]	Slot	$\alpha = 10^\circ$	aerofoil cut back	M = 0.5 and	Coherent temperature profile's and laminar and turbulent coolant flow investigated.
Shinn et al.[27]	Circular	$\alpha = 20^\circ$	flat	VR= 1.414	Effect of micro ramp vortex generator on voracity and effectiveness
Renge et al.[28]	Circular	$\alpha = 30^\circ$	flat	VR= 0.1 and 0.28 and $Re_{ms} = 4 \times 10^5$	Effect of variable density coolant jet on film cooling
Baagherzadeh [29]	Circular	$\alpha = 30^\circ$	flat	M=2 and $Re_{ms} 11000$	LES results show good agreement with experimental data.
Gräf et al. [30]	Circular	$\alpha = 35^\circ$ & $\beta = 45^\circ$	flat	M = 1	The anti-kidney vortex formed by compound hole is investigated.

**Table – 2** Operating parameters considered in the present numerical study.

<b>Parameters</b>	<b>Forward-cylindrical (FCH)</b>	<b>Reverse cylindrical (RCH)</b>	<b>Forward shape(FSH)</b>	<b>Reverse shape (RCH)</b>
$Re_{sec.}$	$0.9 \times 10^3$	$0.9 \times 10^3$	$0.9 \times 10^3$	$0.9 \times 10^3$
Blowing ratio (M)	1	1	1	1
Density ratio (DR)	2.46	2.46	2.46	2.46
$T_{ms}$ (K)	1561	1561	1561	1561
$T_{sec.}$ (K)	644	644	644	644

**Table – 3** Boundary conditions considered in the present numerical study.

<b>Domain Name of Boundary</b>	<b>Forward Cylindrical Hole</b>	<b>Reverse Cylindrical Hole</b>	<b>Forward Shaped Hole</b>	<b>Reversed Shaped Hole</b>
Mainstream inlet	Velocity inlet (Turbulent Profile) at $T_{ms}$			
Secondary inlet	Velocity inlet (Turbulent Profile) at $T_{sec.}$			
Outlet	Pressure Outlet	Pressure Outlet	Pressure Outlet	Pressure Outlet
Side	Periodic	Periodic	Periodic	Periodic
Flat surface				
Top surface				
Hole pipe	No-slip Wall (adiabatic)	No-slip Wall (adiabatic)	No-slip Wall (adiabatic)	No-slip Wall (adiabatic)
Plenum chamber walls				

**Table – 4** The comparison of present non-dimensional grid refinement parameters with the recent LES studies.

S No.	Authors	Non-dimensional grid refinement parameters	Non-dimensional grid refinement parameters (Present LES study)
1	Jiang et al. [45]	$\Delta x^+ < 90; \Delta y^+ = 0.24; \Delta z^+ = 161.8$	$\Delta x^+ < 60; \Delta y^+ < 1; \Delta z^+ < 60$
2	Georgiadis et al. [44]	$50 \leq \Delta x^+ \leq 150; \Delta y^+ < 1; 15 \leq \Delta z^+ \leq 40$	where $\Delta x^+, \Delta y^+$ and $\Delta z^+$ represents
3	Johnson et al. [47]	$\Delta x^+ \sim 35; \Delta y^+ < 1; \Delta z^+ \sim 16$	the non-dimensional grid spacing
4	Pachpute and Premachandran [48]	$\Delta x^+ < 100; \Delta y^+ < 2; \Delta z^+ < 30$	near the wall in the direction tangent to the wall, normal to the wall, and span wise respectively.
5	Babu and Sarkar [49]	$\Delta x^+ \approx 50; \Delta y^+ \approx 1; \Delta z^+ \approx 20$	

Fig. 1 Schematic diagram of film cooling flow with a cylindrical hole [5].

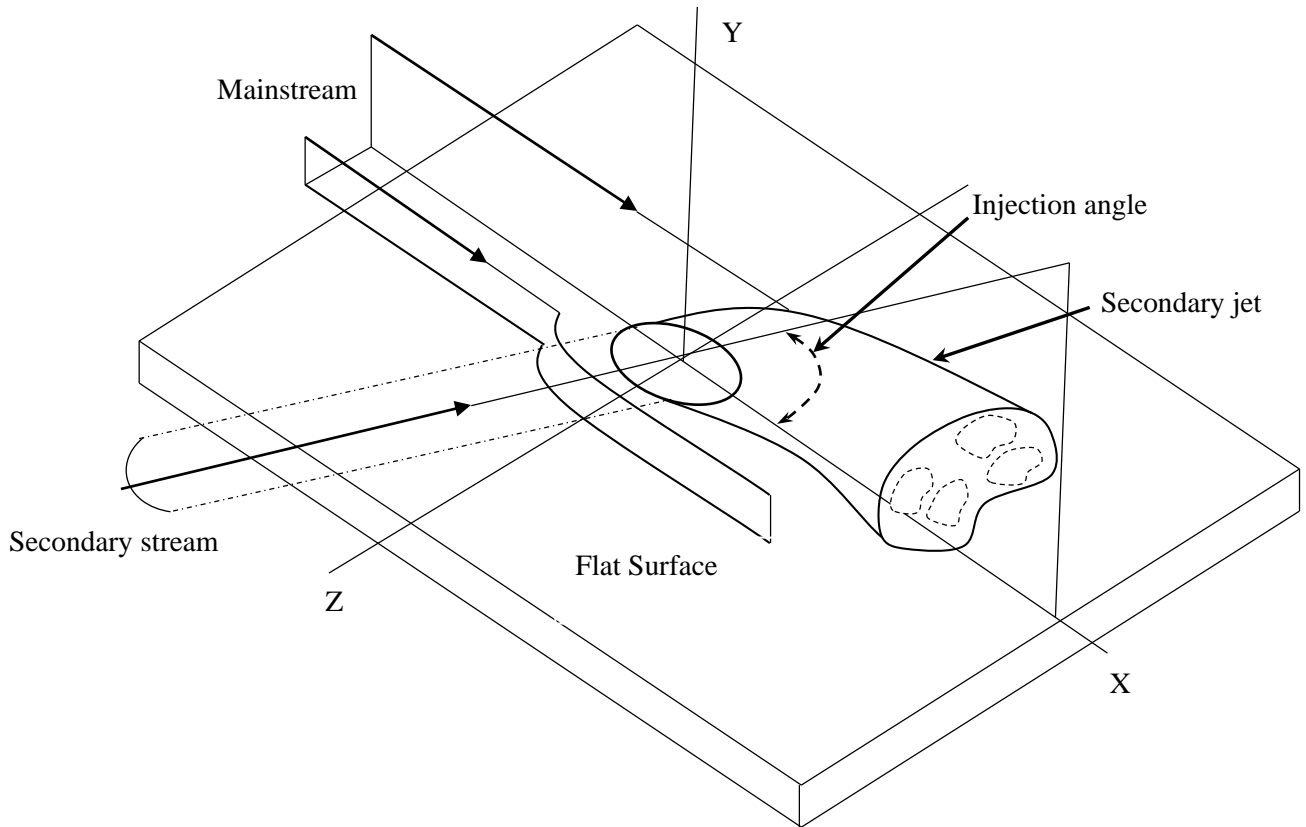


Fig. 2 (a) Three-dimensional domain of film cooling over the flat surface along with boundary conditions: Forward and reverse cylindrical hole.

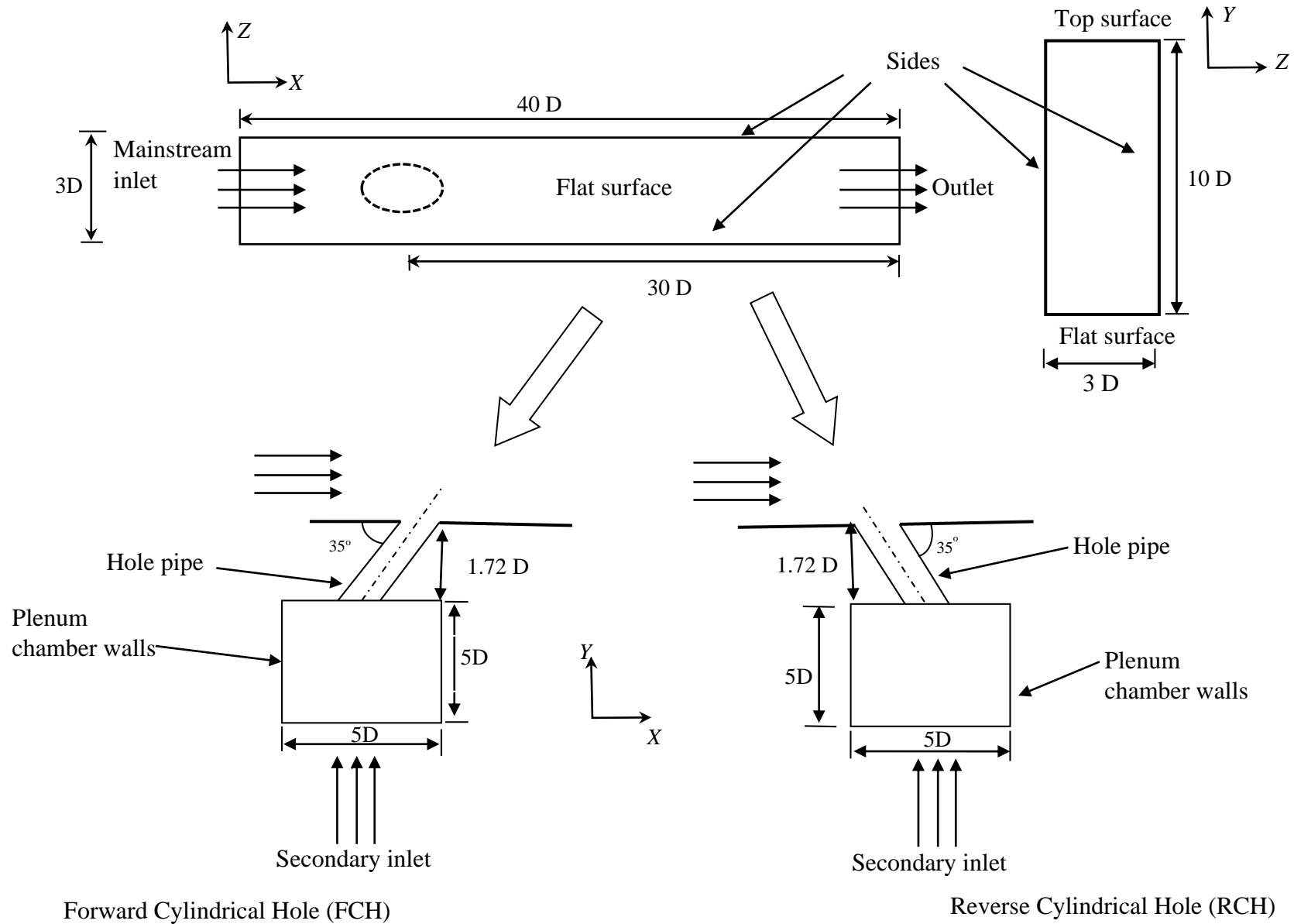


Fig. 2 (b) Three-dimensional domain of film cooling over the flat surface along with boundary conditions: Forward and reverse shaped hole.

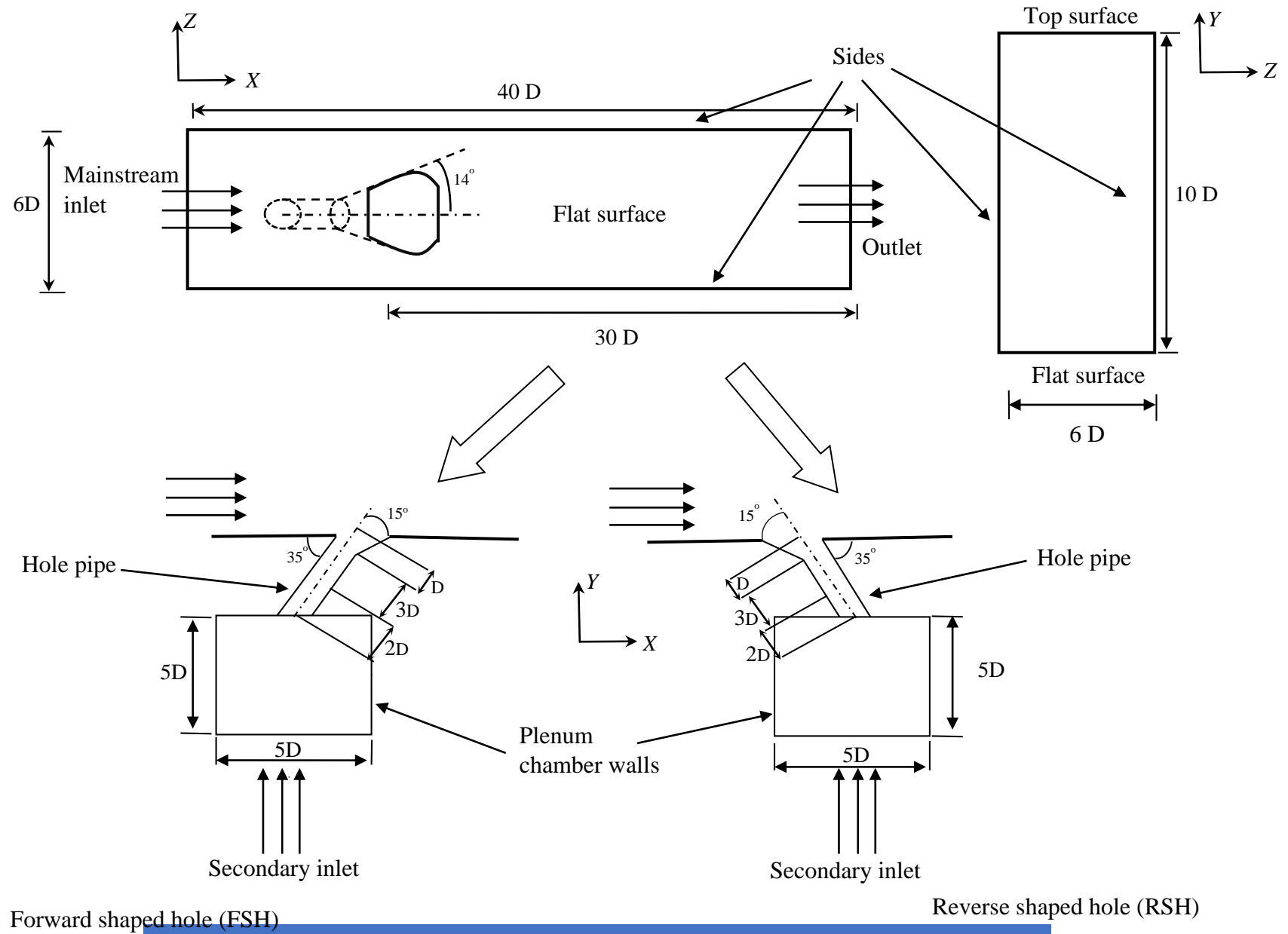
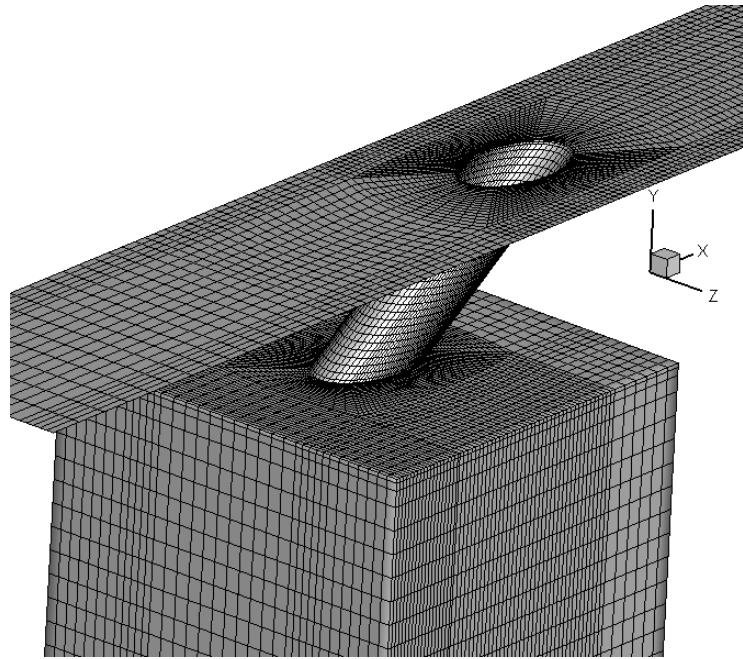
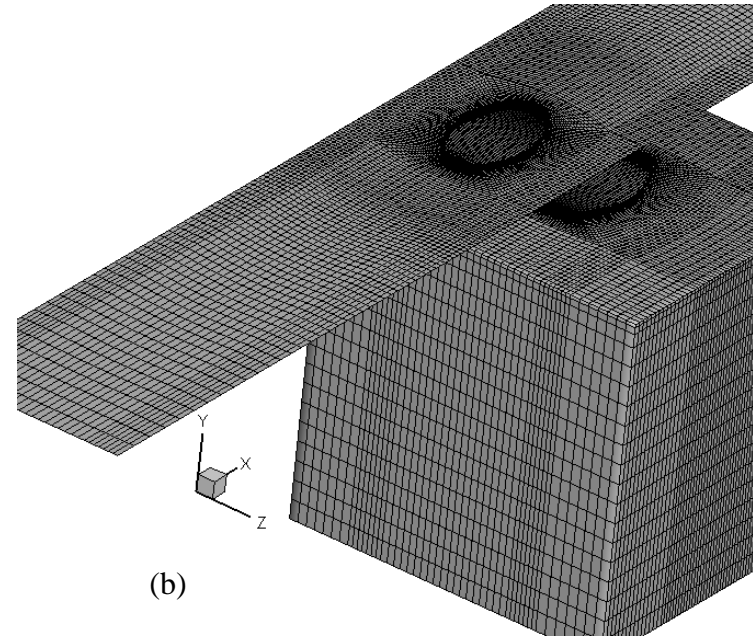


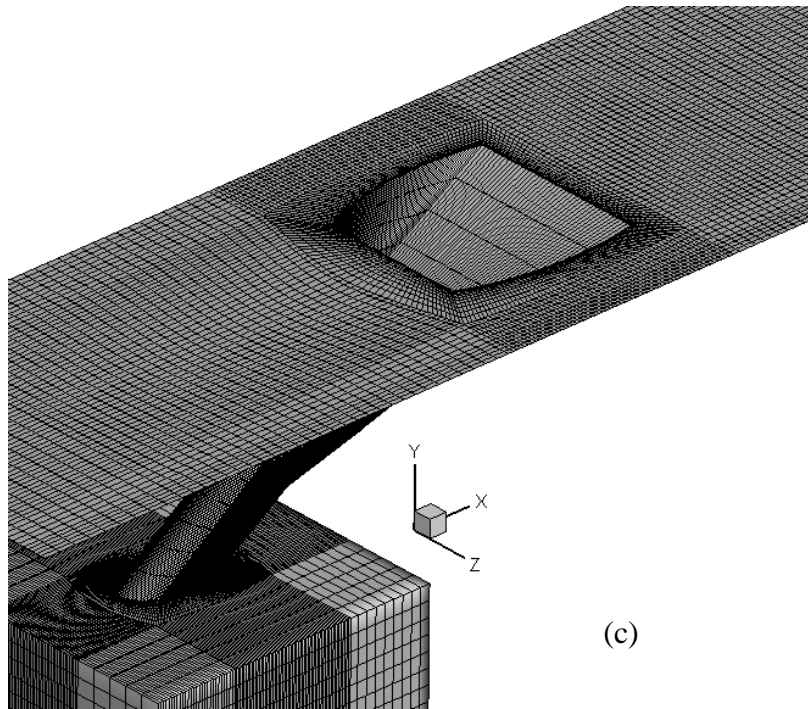
Fig. 3 Typical mesh for 3D computational domain: (a) Forward cylindrical hole (FCH); (b) Reverse hole (RCH); (c) Forward shaped hole (FSH); (d) Reverse shaped hole (RCH).



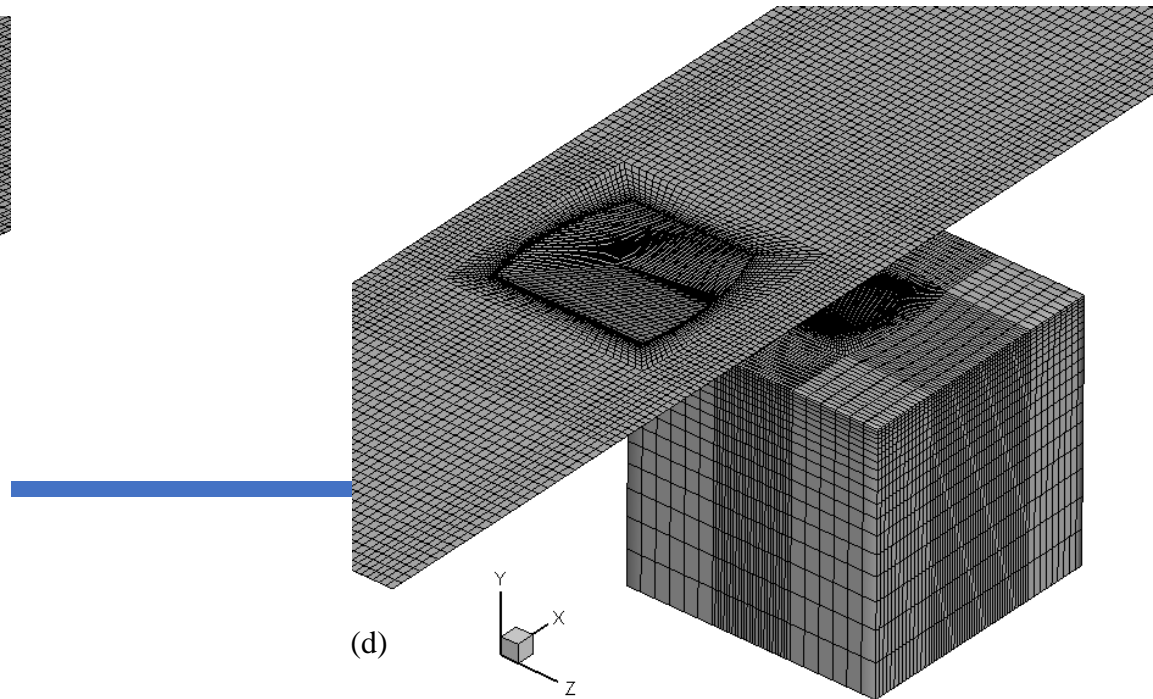
(a)



(b)

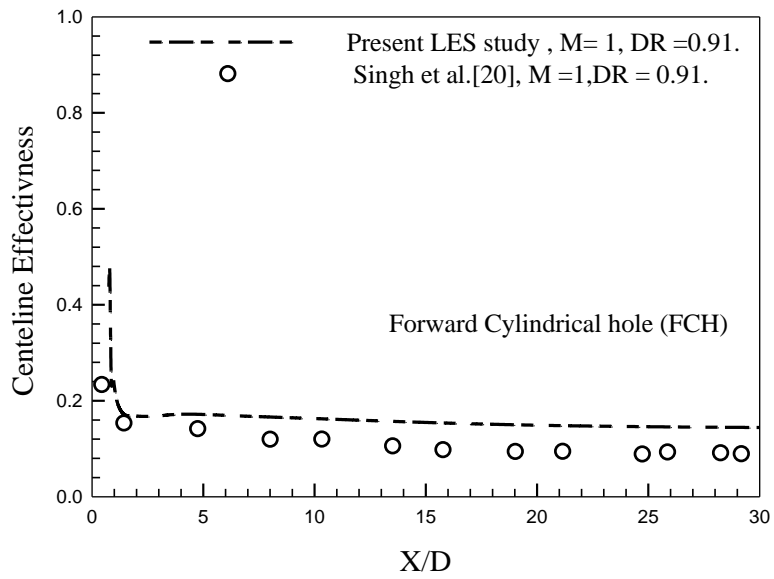


(c)

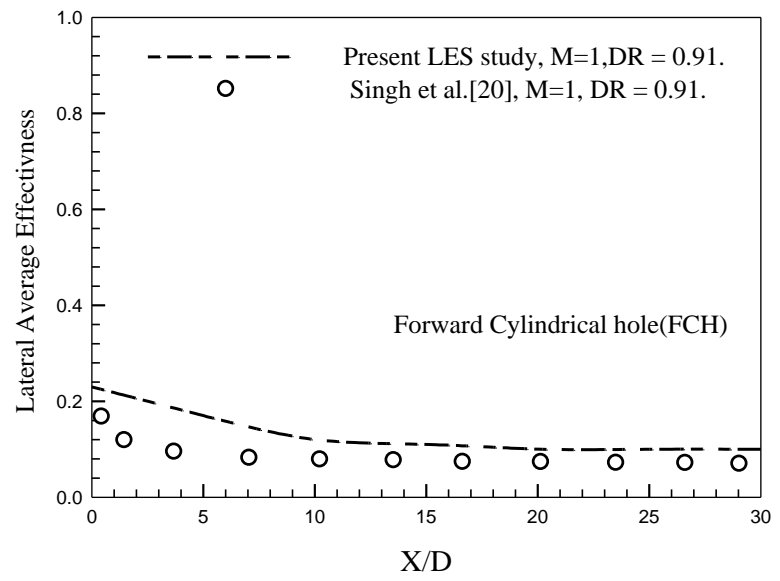


(d)

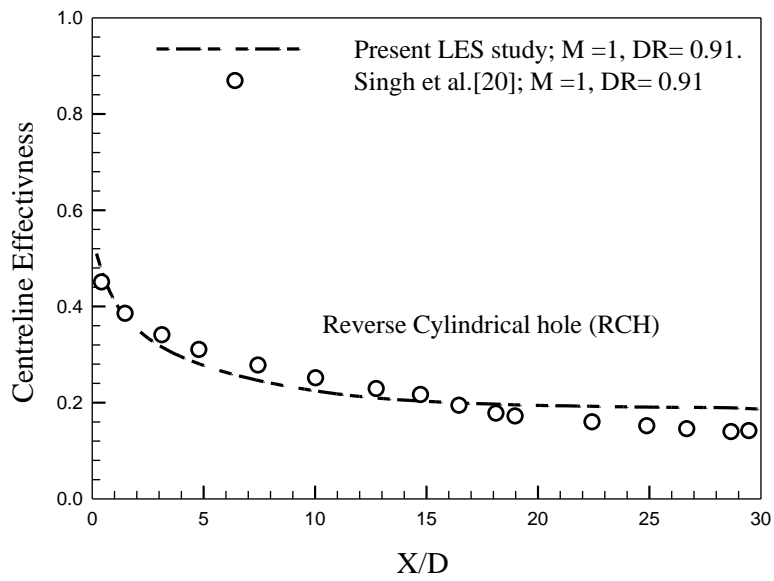
Fig. 4 Comparison of the present numerical result of effectiveness with the experimental results of Singh et al. [20].



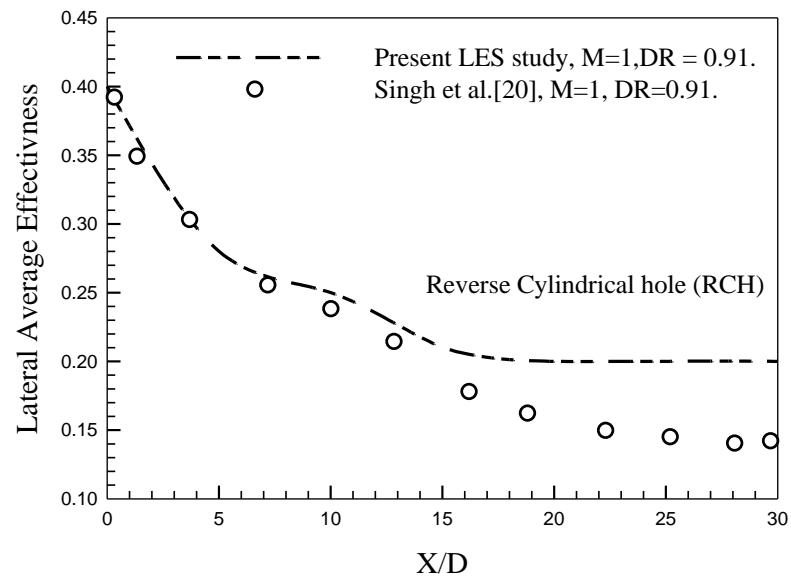
(a)



(b)



(c)



(d)

Fig. 5 Effectiveness plot for various hole configurations: (a) Centreline effectiveness; (b) Lateral average effectiveness (cylindrical holes); (c) Lateral average effectiveness (shaped holes).

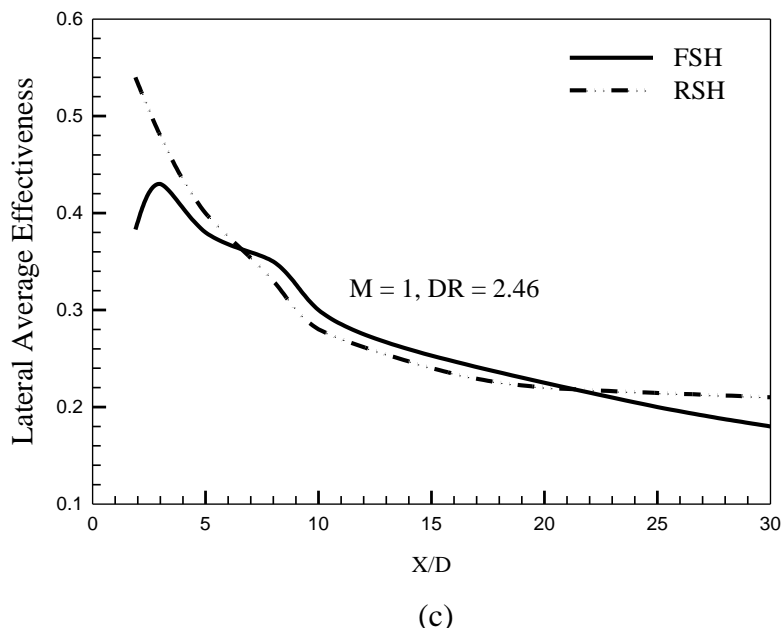
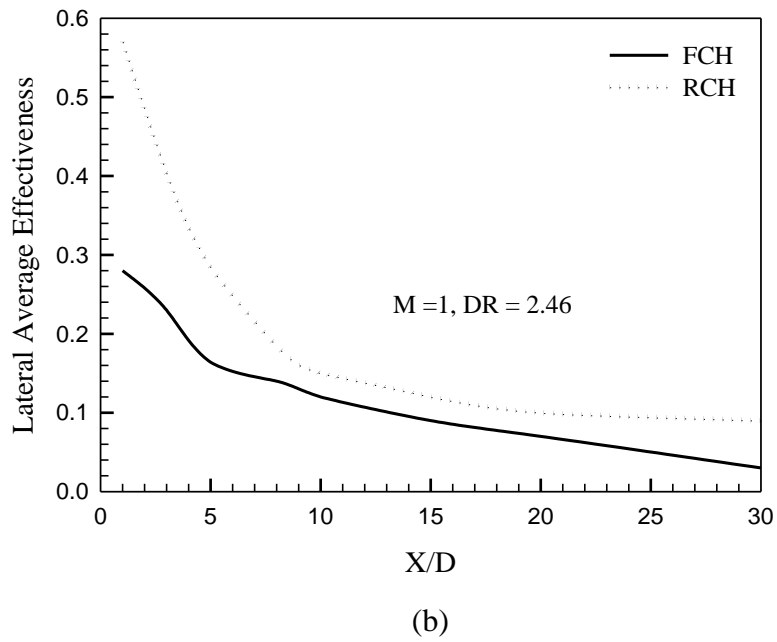
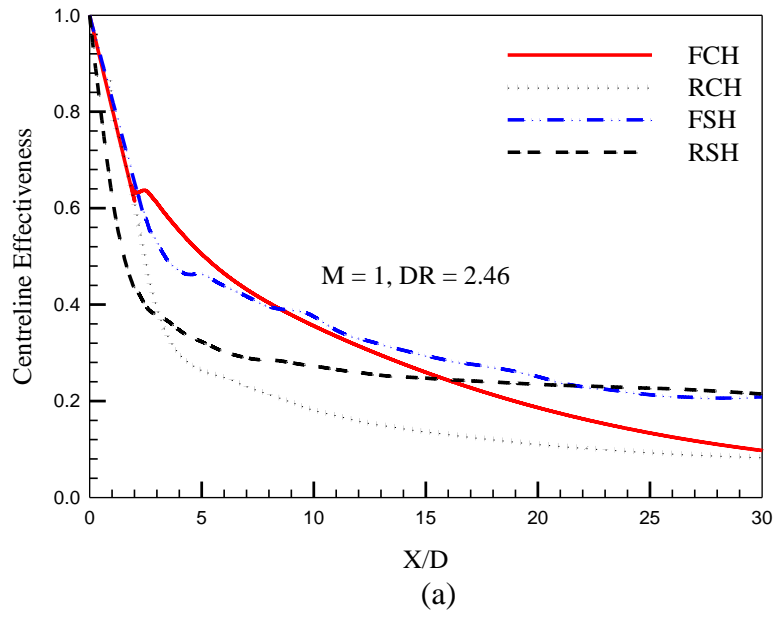
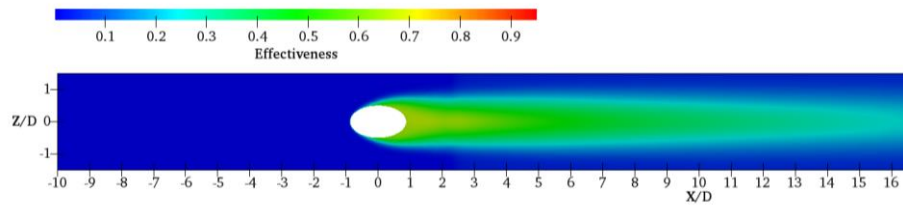
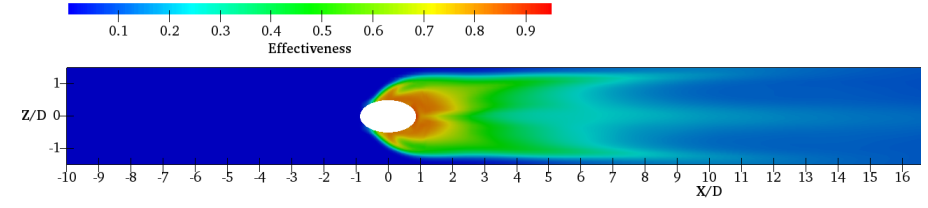


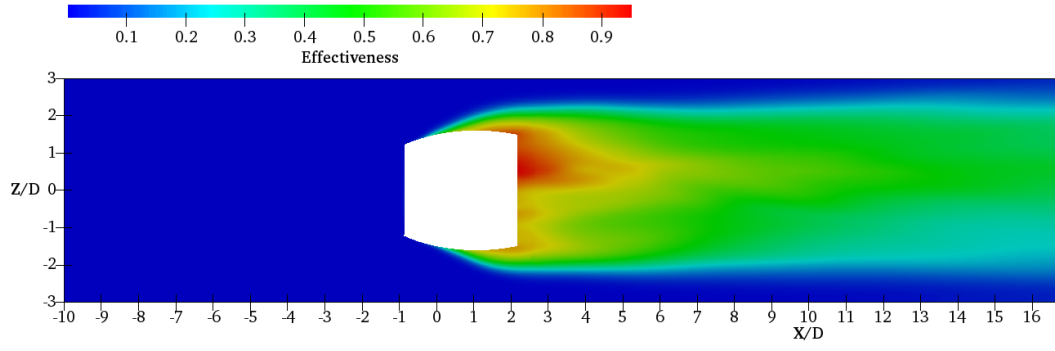
Fig. 6 Effectiveness contours of various hole configurations: (a) Effectiveness contour (FCH); (b) Effectiveness contour (RCH); (c) Effectiveness contour (FSH); (d) Effectiveness contour (RSH).



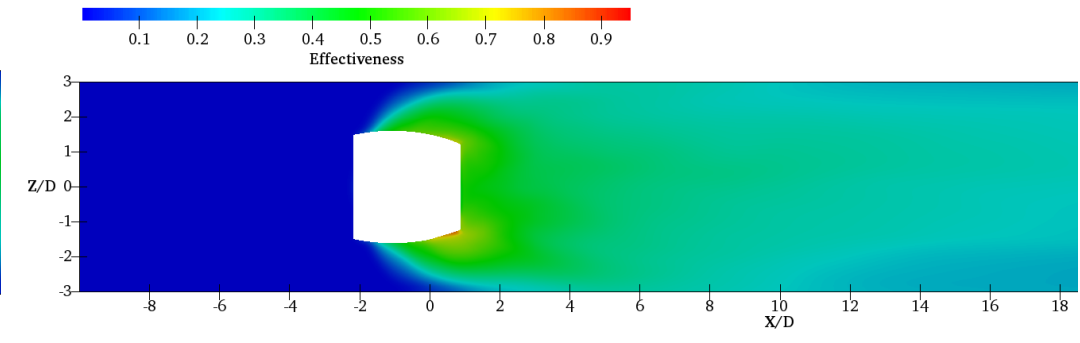
(a)



(b)

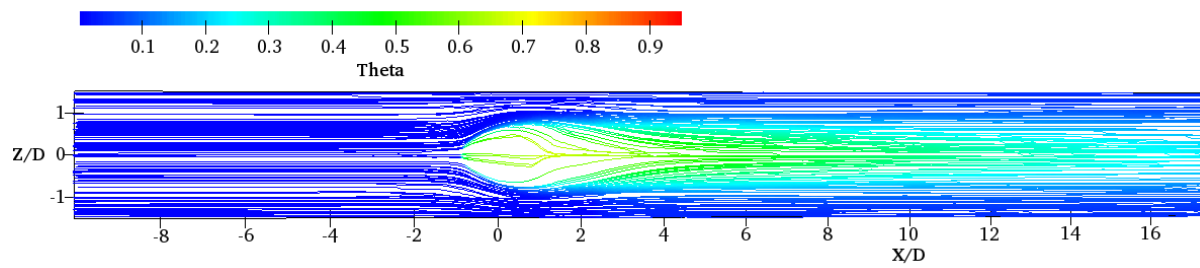


(c)

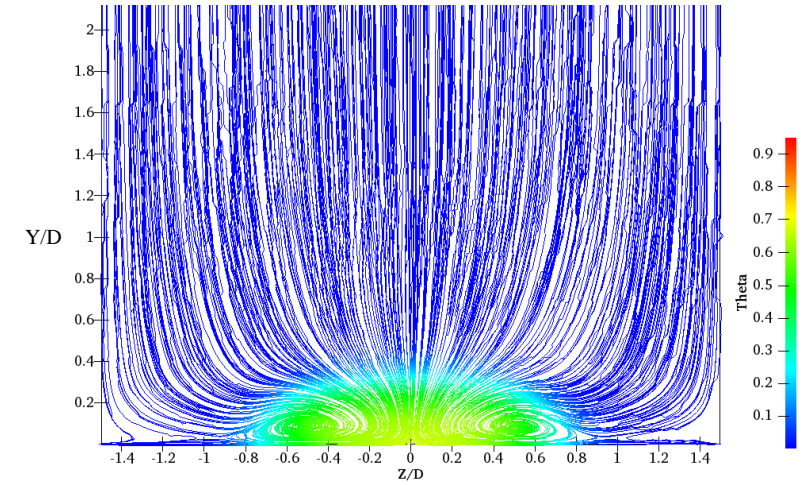


(d)

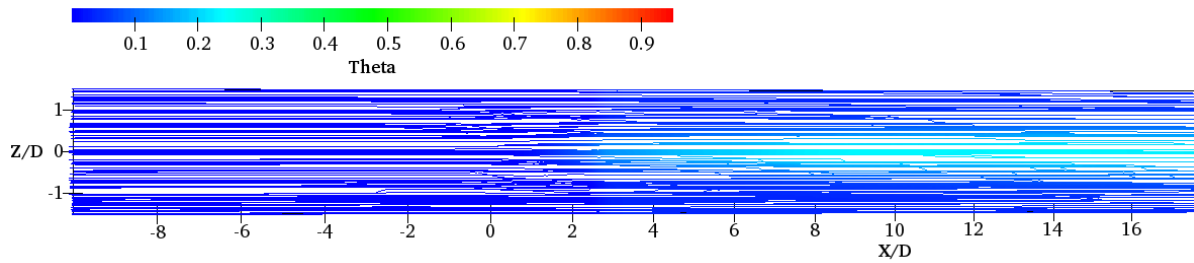
Fig. 7 Streamline contours of non-dimensional temperature ( $\theta$ ) for FCH: (a)  $Y/D = 0$ , (X-Z plane); (b)  $X/D = 1$ , (Y-Z plane); (c)  $X/D = 3$ , (Y-Z plane); (d)  $Y/D = 0.5$ , (X-Z plane).



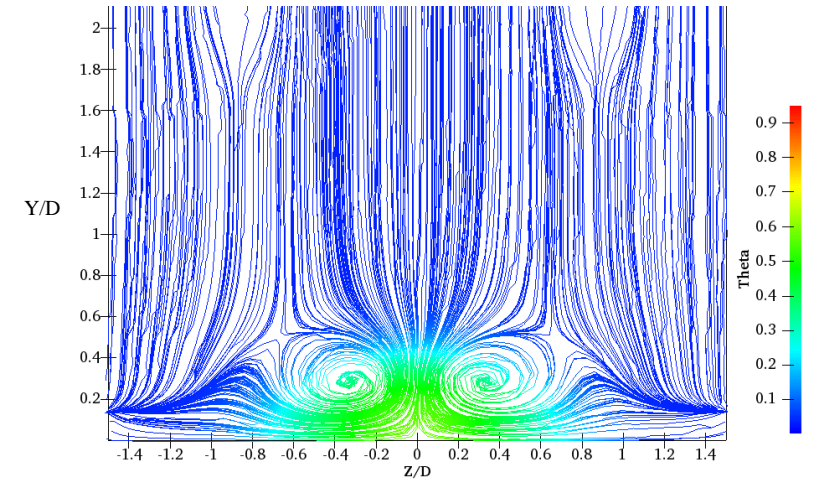
(a)



(b)

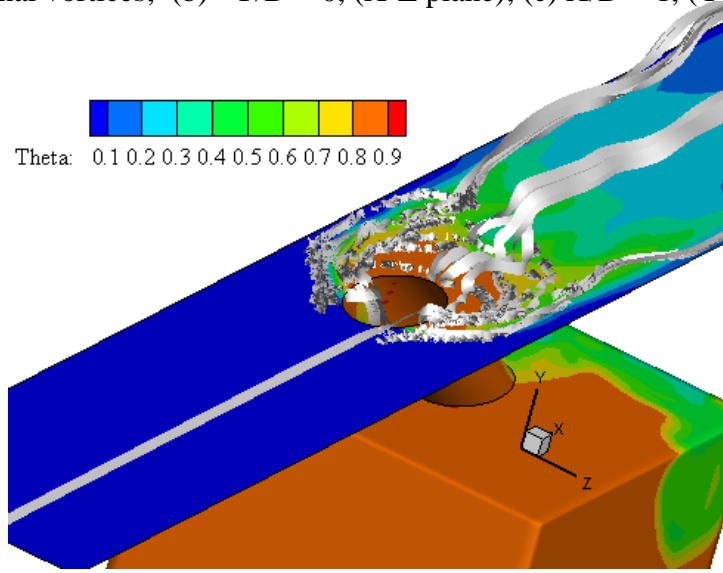


(d)

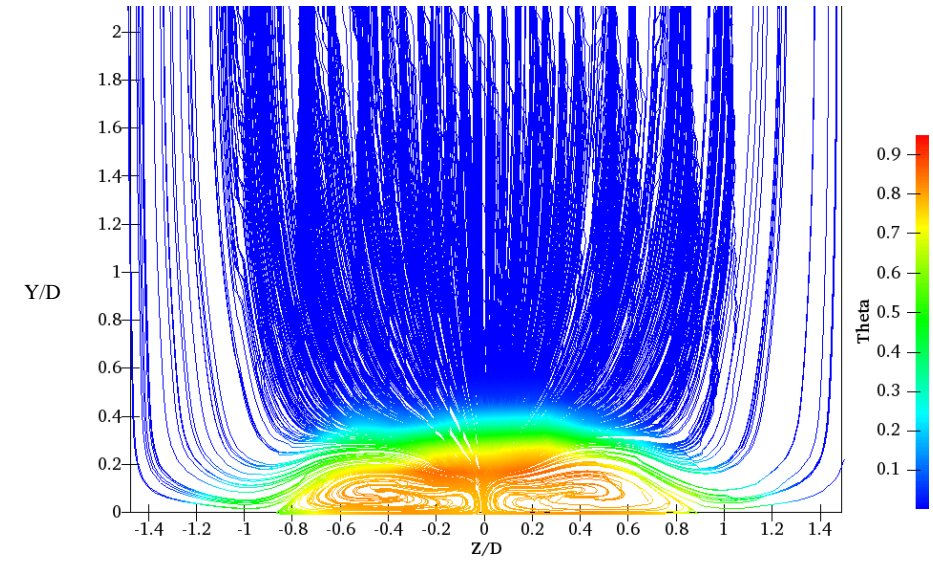


(c)

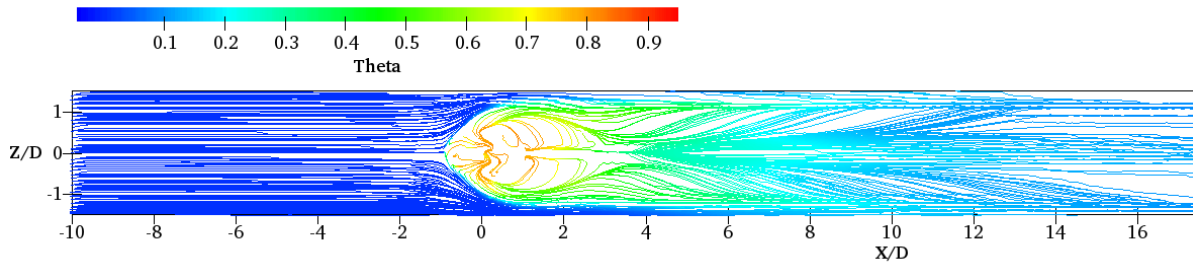
Fig. 8 Streamline contours of non-dimensional temperature ( $\theta$ ) for RCH at Streamline contours of non-dimensional temperature ( $\theta$ ) for FCH: (a) Three dimensional vortices; (b)  $Y/D = 0$ , (X-Z plane); (c)  $X/D = 1$ , (Y-Z plane); (d)  $X/D = 3$ , (Y-Z plane); (e)  $Y/D = 0.5$ , (X-Z plane).



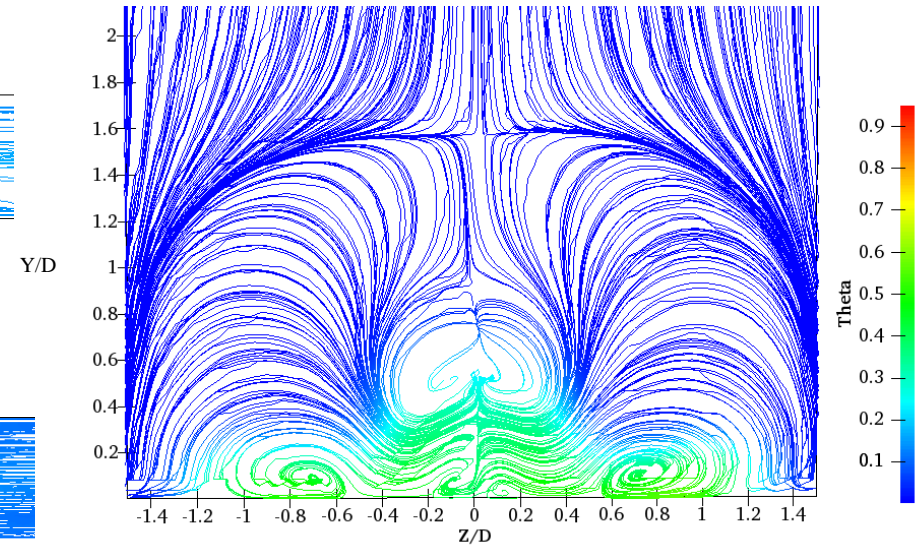
(a)



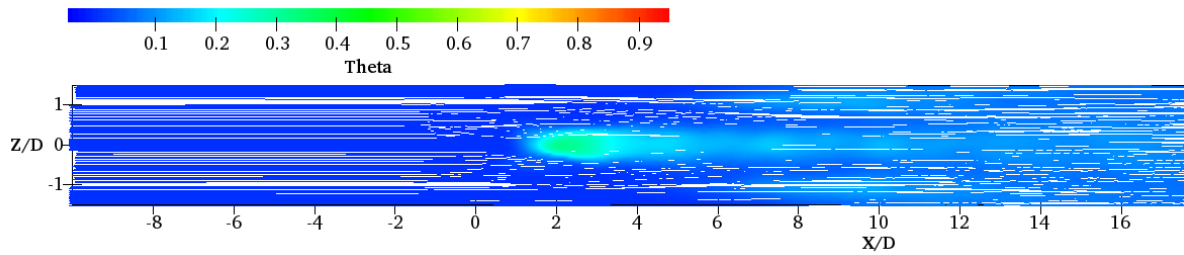
(c)



(b)

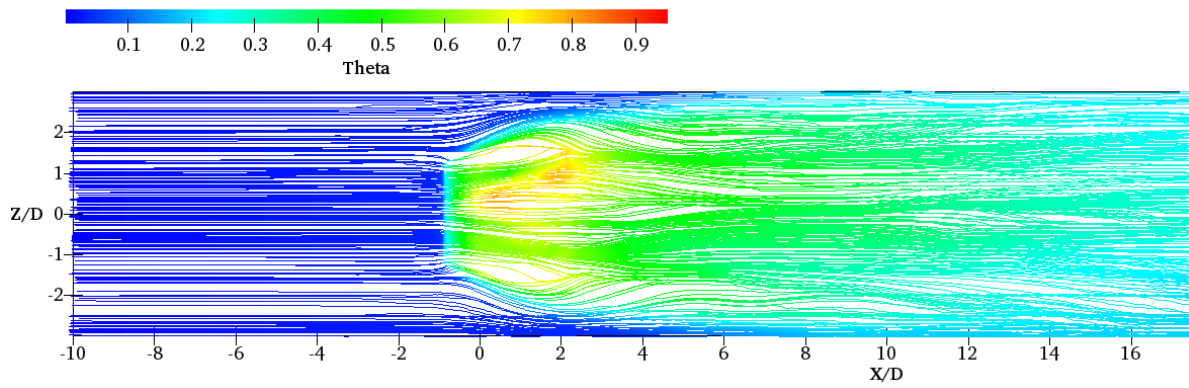


(d)

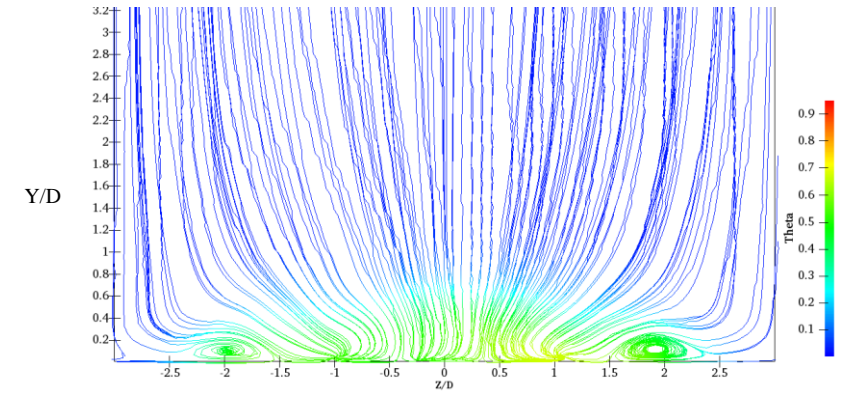


(e) DUSHYANT SI EA-20-1180

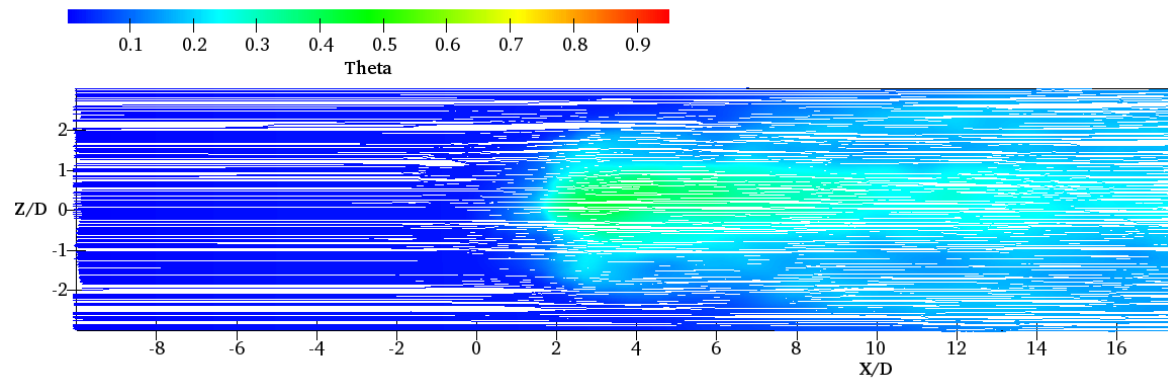
Fig. 9 Streamline contours of non-dimensional temperature ( $\theta$ ) for FSH: (a) Streamline contours of non-dimensional temperature ( $\theta$ ) for FCH: (a)  $Y/D = 0$ , (X-Z plane); (b)  $X/D = 2$ , (Y-Z plane); (c)  $X/D = 5$ , (Y-Z plane); (d)  $Y/D = 0.5$ , (X-Z plane).



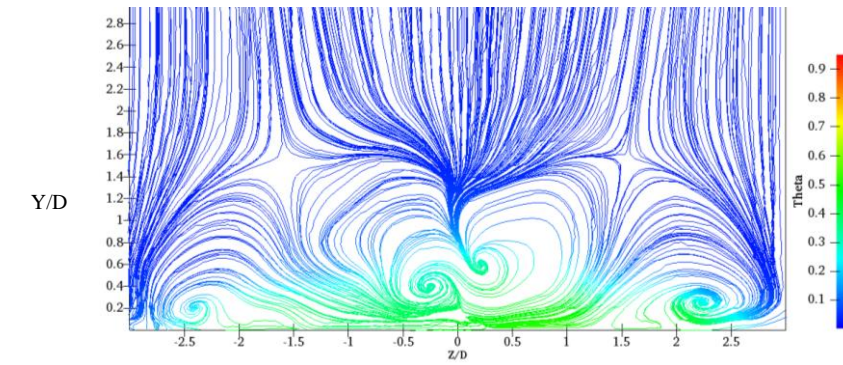
(a)



(b)



(d)



(c)

Fig. 10 Streamline contours of non-dimensional temperature ( $\theta$ ) for RSH and FCH: (a) Three-dimensional vortices; (b)  $Y/D = 0$ , (X-Z plane); (c)  $X/D = 2$ , (Y-Z plane); (d)  $X/D = 5$ , (Y-Z plane); (e)  $Y/D = 0.5$ , (X-Z plane).

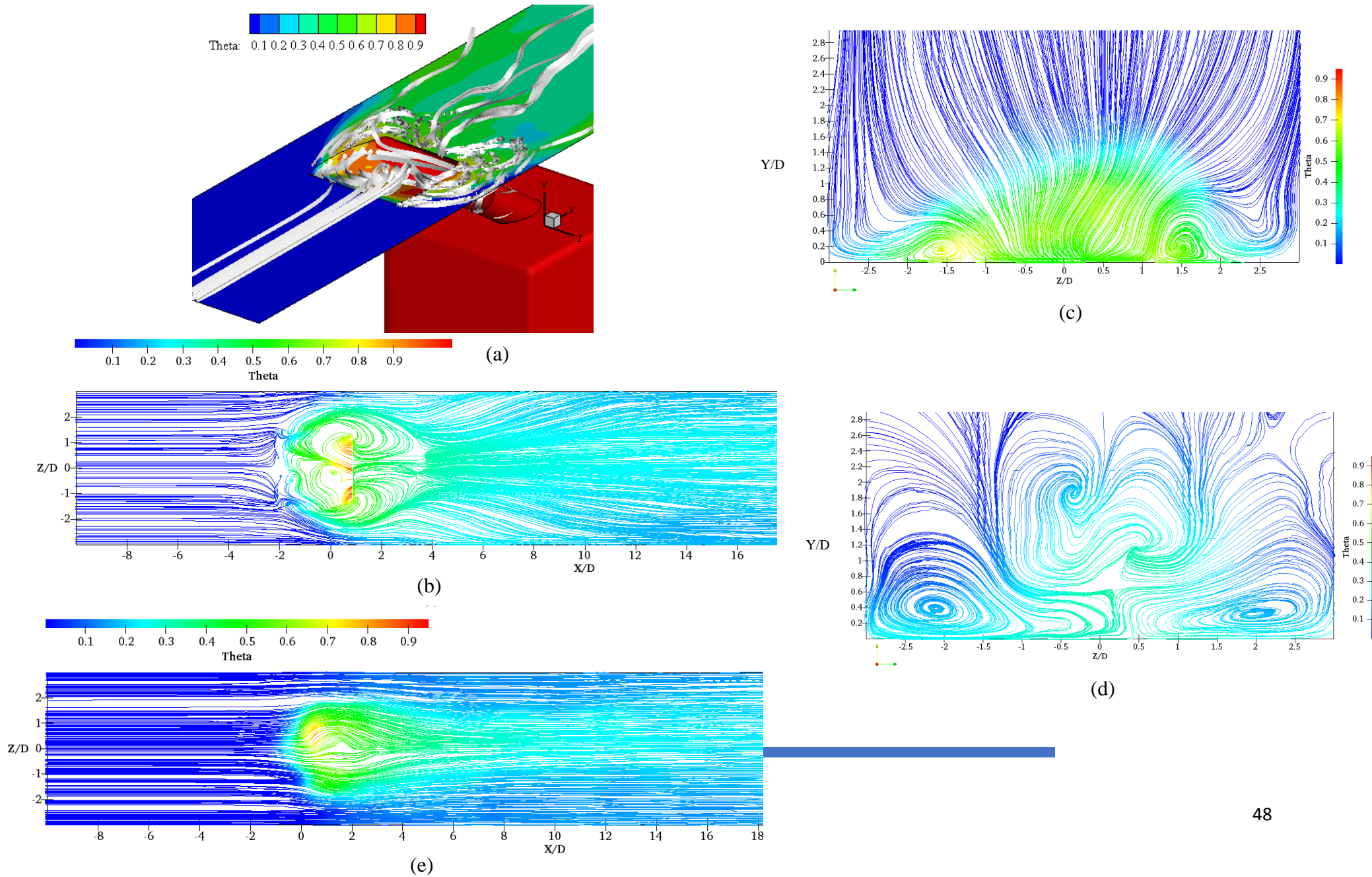
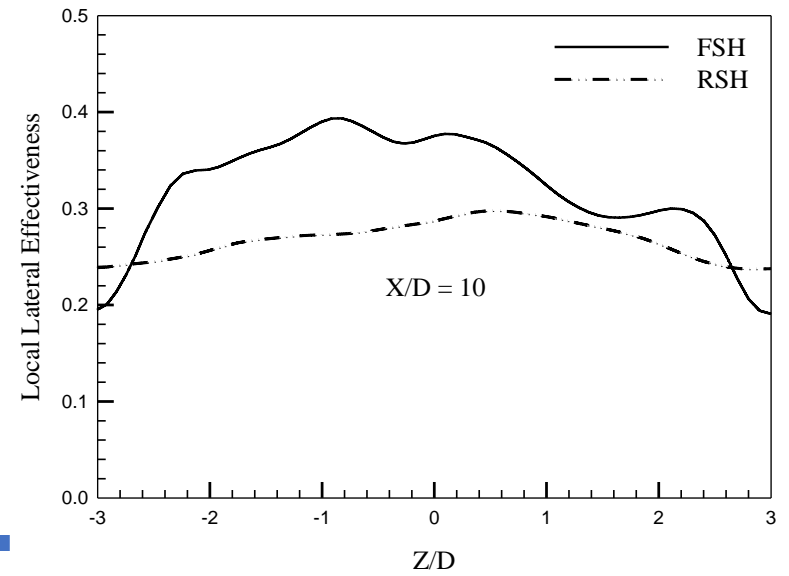
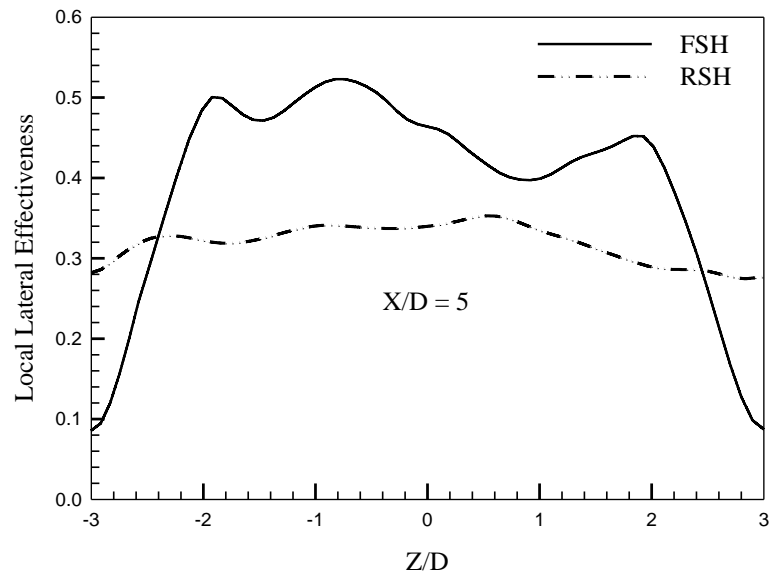
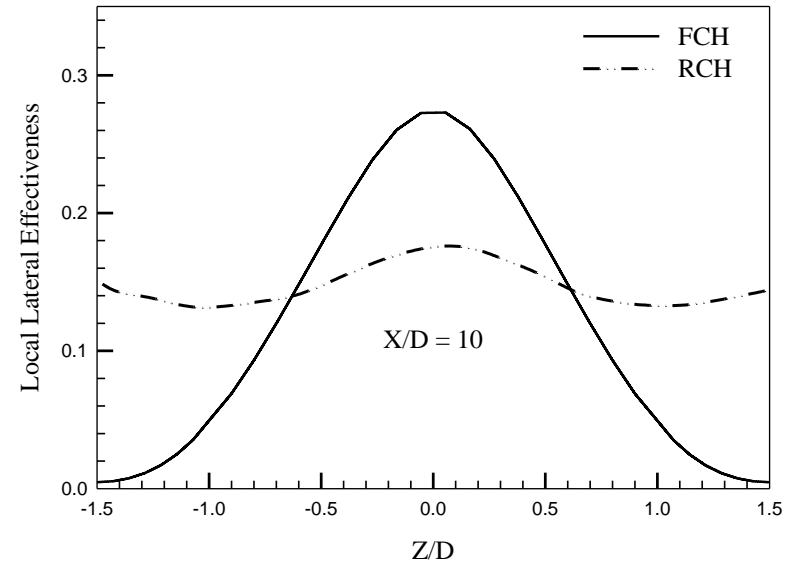
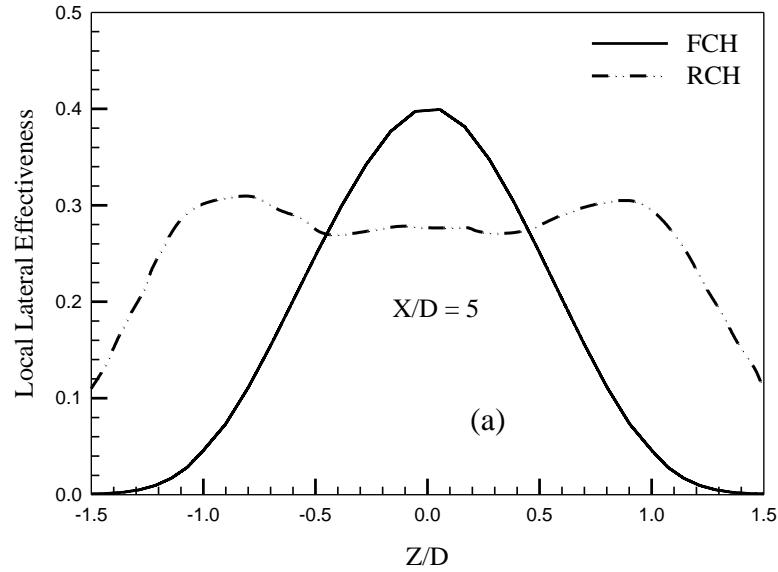


Fig. 11 Local lateral effectiveness contours: (a) FCH and RCH at  $X/D = 5$ ; (b) FCH and RCH at  $X/D = 10$ ; (c) FSH and RSH at  $X/D = 5$ ; (d) FSH and RSH at  $X/D = 10$ .



DUSHYANT SINGH, TSEA – 20- 1180

(c)

(d)

Fig. 12 Comparison of non-dimensional velocity profiles of various hole configuration at centreline along the Y/D direction at various stream wise locations ( $X/D = 0, 1, 1.5, 2$ ) with PIV results from reference [28].

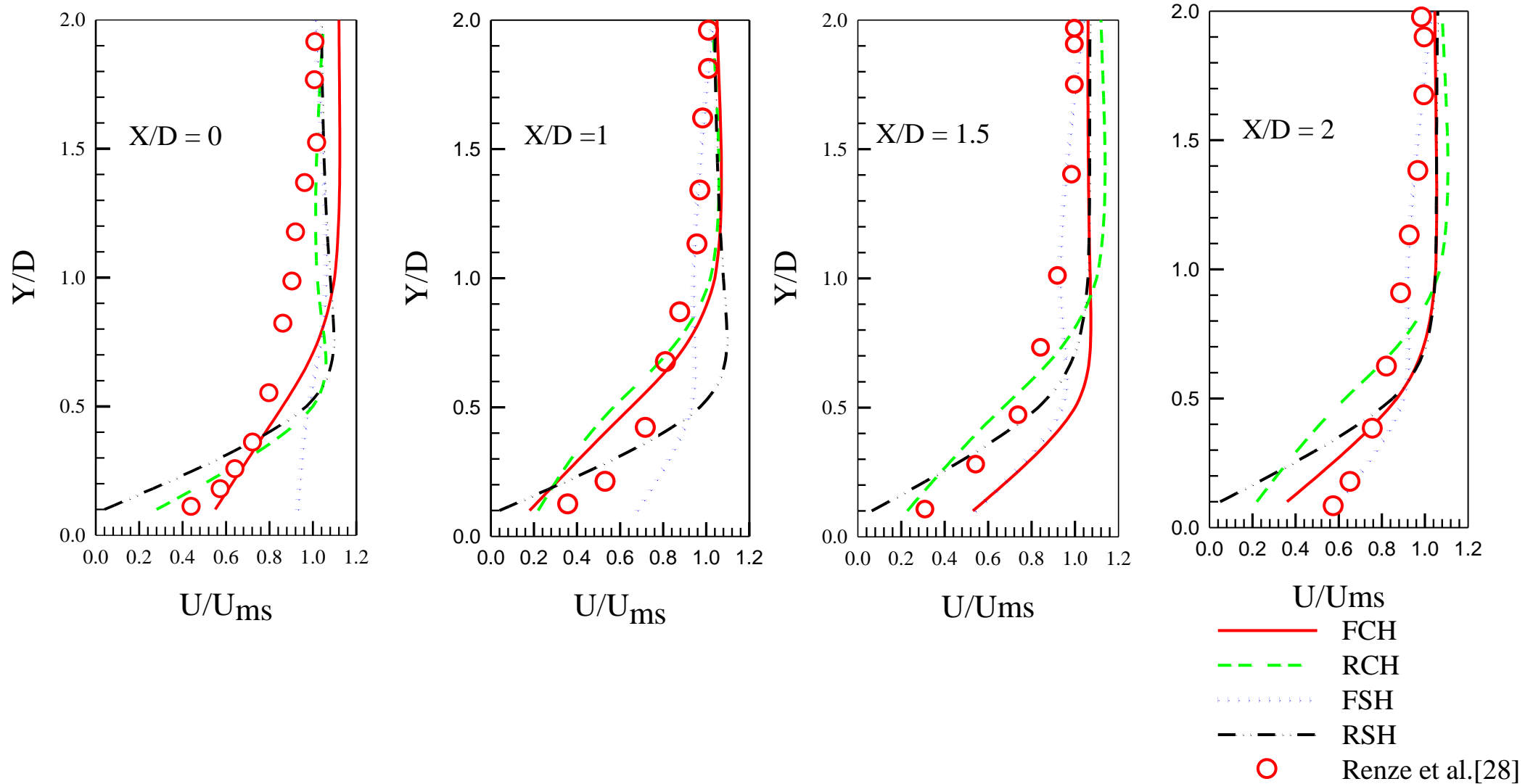


Fig. 13 Comparison of discharge coefficient (Cd) of various hole configurations.

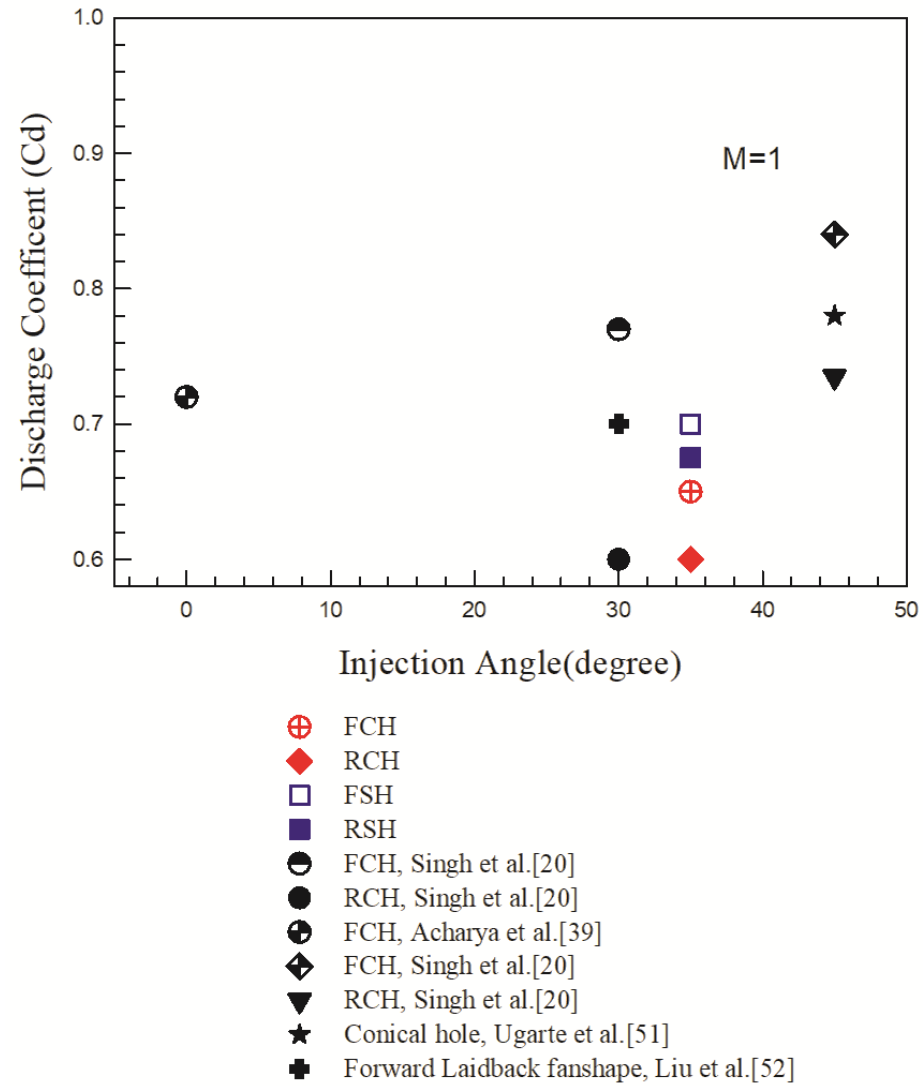


Fig. 14 Non-dimensional velocity contours at flow exit from hole for various hole configurations: (a) FCH; (b) RCH; (c) FSH; (d) RSH.

